KLOE note n. 203

JULY 2005

Direct measurement of the K_L lifetime

G. Lanfranchi

Laboratori Nazionali di Frascati dell'INFN, Frascati

August 3, 2005

Abstract

We present a direct measurement of the K_L lifetime with the $K_L \to \pi^0\pi^0\pi^0$ decays tagged by $K_S \to \pi^+\pi^-$ events. We used a data sample of ~ 400 pb^{-1} of integrated luminosity collected by KLOE during 2001 and 2002 runs. With a fit of the proper time distribution we measure $\tau = (50.92 \pm 0.17_{\rm stat} \pm 0.25_{\rm syst})$ ns. The K_L tagging procedure, the decay vertex reconstruction algorithm and the signal selection procedure are described. The impact of the lifetime measurement on the determination of the CKM element $|V_{us}|$ from K_L semileptonic decays is also discussed.

Contents

1 Introduction

The K_L lifetime is necessary to determine all the partial decay widths of the K_L from the measured branching ratios and, in particular, to extract the CKM matrix element $|V_{us}|$ from K_L semileptonic decays. The determination of $|V_{us}|$ from K_L semileptonic decays is dominated by the error on the measurement of the K_L lifetime. This is based on a single direct measurement that was performed more than 30 years ago [1].

The measurement of the K_L lifetime is hard because the K_L lives ~ 50 ns and can not be stopped. Moreover the knowledge of the momentum spectrum is required.

KLOE is the ideal experiment to perform again such a measurement since the K_Lś are almost monochromatic[1] and with very low momentum ($p \sim 110$ MeV/c) and, therefore, a large fraction of them ($\sim 50\%$) decays inside the detector.

The statistical error on the lifetime depends on the number of events, $\propto 1/\sqrt{N}$ and, very strongly, on the time interval covered (Ref. [2]):

$$\frac{\delta\tau}{\tau} = \frac{1}{\sqrt{N}} \times \left[\frac{-1 + e^{3T} + (e^T - e^{2T})(3 + T^2)}{(-1 + e^T)^3}\right]^{-0.5} \tag{1}$$

where $T = \Delta t/\tau$ is the time interval covered by the fit in lifetime units and N is the number of events in that interval.

The Equation 1 comes from the well known formula that gives the statistical accuracy reachable on a parameter p when a set of N measurements have been done on the physical quantity x, once the distribution function $f(x;p)$ is known:

$$\sigma_p = \sqrt{-\frac{1}{\frac{\partial^2 W}{\partial p^2}|_{p=\overline{p}}}}$$

where $W = log\mathcal{L}$, $\mathcal{L} = \prod f(x_i;p)$ is the likelihood function and $\overline{p}$ is the best estimate for p which maximises the $\mathcal{L}$. In our case $f(x;p) = e^{-t/\tau}$.

The behaviour of the Eq. 1 is shown in Fig. 1 in case of constant number of events N, (left) and with $N \propto T$ (right), which is approximately correct for small T.

With $T \sim 0.4$ and $N \sim 9 \cdot 10^6$ (which is the KLOE case) we can get, in principle, a statistical error of $\sim 0.3\%$. The KTeV and NA48 experiments, where the kaon momentum spectrum ranges from 70 GeV and 170 GeV, can reach something in between $T = 0.5\%$ and $T = 5\%$ depending on the fiducial volume and K_L mmomentum. Therefore they should collect respectively $\times 5000$ (for T=0.5%) and $\times 100$ (for T=5%) more events to reach the same statistical accuracy.

We have measured the K_L lifetime using the fully neutral decay $K_L \to \pi^0\pi^0\pi^0$ tagged by $K_S \to \pi^+\pi^-$ events. This choice is motivated by the fact that we want to

[1] ϕ mesons at DAΦNE are produced almost at rest with a small horizontal momentum of about 12.6 MeV/c.

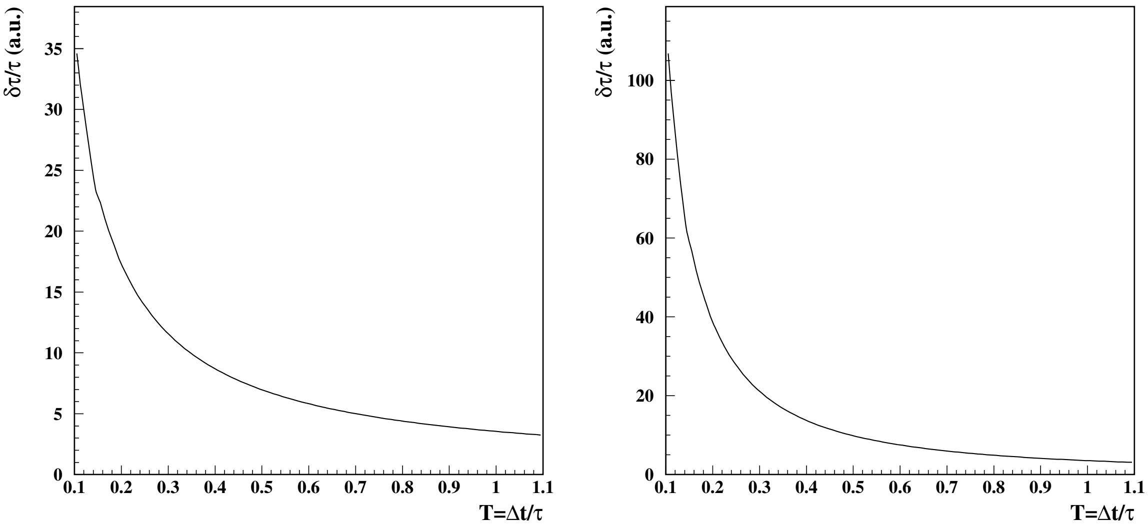

Figure 1: Lifetime statistical error in arbitrary units as a function of the fitted interval, in lifetime units. Left: for a constant number of events. Right: for $N \propto T$.

maximize the number of tagged events to reduce the statistical error and, simultaneously, we want to avoid any coupling among tagging and tagged events in order to minimize the systematic uncertainty.

2 Data and Monte Carlo samples

We used ~ 150 pb^{-1} of the data collected in 2001 and ~ 250 pb^{-1} of the data collected in 2002 for a total of ~ 400 pb^{-1}. The Monte Carlo sample consists of ~ 500 pb^{-1} of equivalent integrated luminosity.

A very loose preselection is performed requiring a tagging $K_S \to \pi^+\pi^-$ event plus at least two clusters on the calorimeter not associated to a track[2]. This preselection allows to have in the same filtered sample both $K_L \to \pi^0\pi^0\pi^0$ and $K_L \to \pi^+\pi^-\pi^0$ events and use the latter as control sample to evaluate systematic uncertainties.

3 Tag and bunch crossing identification

The $K_L \to \pi^0\pi^0\pi^0$ events are tagged using $K_S \to \pi^+\pi^-$ decays. $K_S \to \pi^+\pi^-$ events are identified by requiring two tracks of opposite charge, that form a vertex within r_t <10 cm and $|z| < 20$ cm with respect the interaction point[3] (IP), have a total momentum in the ϕ rest frame within 10 MeV/c with respect to the nominal one and

[2] A cluster associated to a track must be found within a sphere of radius of 50 cm with respect to the estrapolation point of a given track to the calorimeter.

[3] If more than one vertex is present the closest one is kept.

form an invariant mass M in the $\pi^+\pi^-$ hypothesis within $|M - M_K| < 5$ MeV (Fig. 2). The efficiency on the signal after these two cuts is, from Monte Carlo, $\epsilon \sim 68\%$.

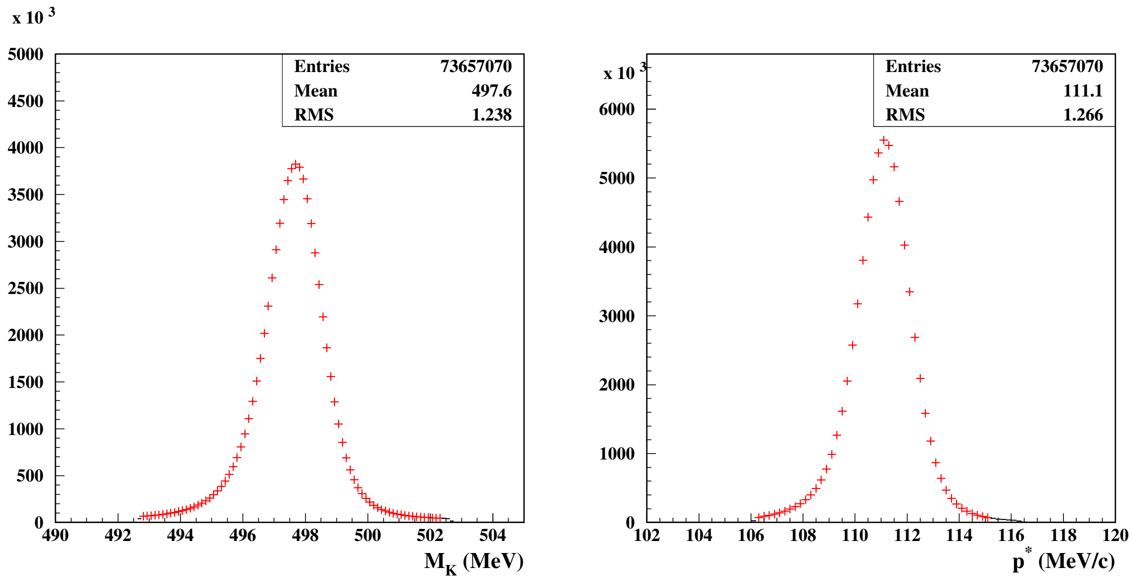

Figure 2: Invariant mass (left) and total momentum in the ϕ rest frame (right) of $K_S \rightarrow \pi^+\pi^-$.

Moreover, at least one of the two tracks must have an associated cluster in the calorimeter in order to reconstruct the event-start time (t_0). The procedure for the determination of the t_0 of each event is described in detail in Ref. [3]. The cluster must have an energy $E \geq 50$ MeV.

To run at the design luminosity, DAΦNE can operate with 120 bunches per ring, which corresponds to a bunch-crossing period T equal to the machine RF period, $T = 2.715$ ns. In practice, during the 2001-2002 data taking period, the bunch crossing period was two times the nominal one, i.e. $T = 5.43$ ns. Due to the large spread of particle arrival times and short bunch-crossing period, the trigger time does not identify the bunch crossing that produces an event; the time at which this bunch crossing occurred must, therefore, be determined offline.

In the case of $K_S \rightarrow \pi^+\pi^-$ selected events the t_0 of each event can be reconstructed by using the time of arrival t of a pion on the calorimeter and the corresponding track length L and speed $\beta\gamma = p/M_\pi$.

In Fig. 3 (left), we show the distribution of $t - L/\beta c$ of one of the two pions from K_S before the t_0 correction: the bunch-crossing structure is clearly visible with a period of T = 5.43 ns.

With such a bunch-crossing period, $\sim 100\%$ correct bunch identification is reached without any further quality requirement on the identified pion tracks. The t_0 is used to correct all the measured times of arrival of the particles on the calorimeter. The accuracy of this procedure is studied using $K_L \rightarrow \pi^+\pi^-\pi^0$ events. In case of correct bunch-crossing identification the following equation must hold:

$$t_\gamma = \frac{L_K}{\beta c} + \frac{L_\gamma}{c}$$

where t_γ is the time of arrival of one of the photons from π^0 on the calorimeter, L_K and β is the path length and speed of the K_L, L_γ is the path length of the photon and c is the light speed.

L_K is known from the position of the vertex reconstructed by the two charged pions and L_γ is reconstructed from the position of the K_L vertex and the impact point of the photon on the calorimeter. The $(t_\gamma - L_K/\beta c - L_\gamma/c)$ distribution is shown in Fig. 3 (right). In case of correct bunch crossing identification this distribution must be peaked at zero while, in the case of wrong bunch identification, peaks at multiples of the bunch crossing period show up: this second case occurs less than 0.1 % of the times (Fig. 3).

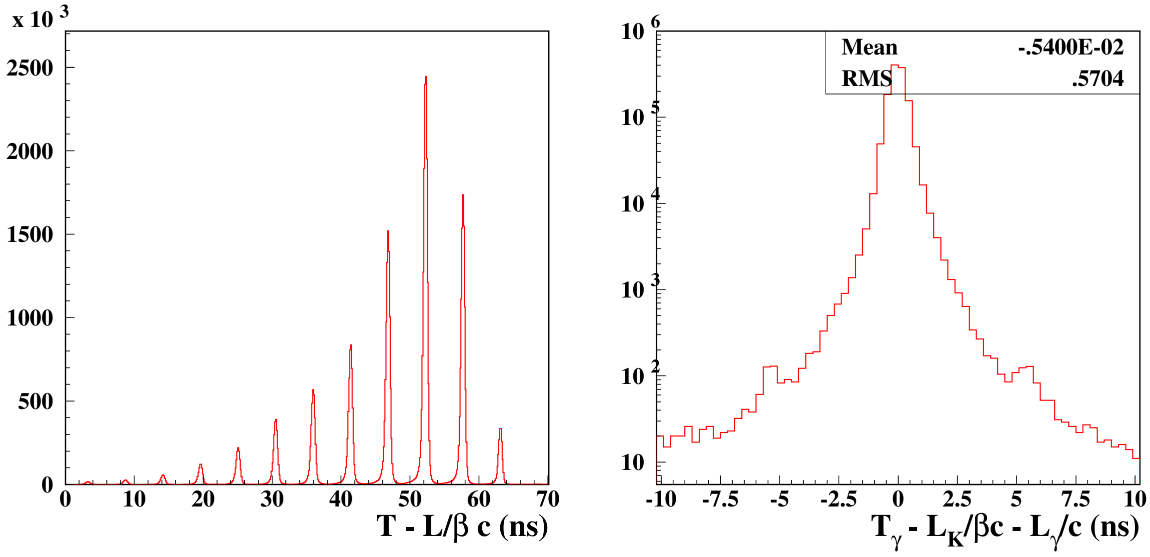

Figure 3: Left: $t - L/\beta c$ of one of the two pions from K_S before t_0 correction. Right: $T_\gamma - L_K/\beta c - L_\gamma/c$ of one photon from $K_L \to \pi^+\pi^-\pi^0$ events after t_0 correction: the two small peaks centred at $\pm$ 5.43 ns give the percentage of wrong reconstructed bunch crossings.

The momentum of the K_L (Fig. 4, left) is measured from the momentum of the K_S (measured from $\pi^+\pi^-$ tracks event by event) and from the momentum of the ϕ (measured with Bhabha events run by run, Fig. 4, right).

The flight direction of the K_L is determined with a resolution on the azimuthal angle of $\sim$1.6° and on the polar angle of $\sim$1.85° (Fig. 5). The angular resolutions have been measured with $K_L \to \pi^+\pi^-\pi^0$ events by comparing the flight direction obtained with the K_L decay vertex and IP positions with the one reconstructed by K_S and ϕ momenta.

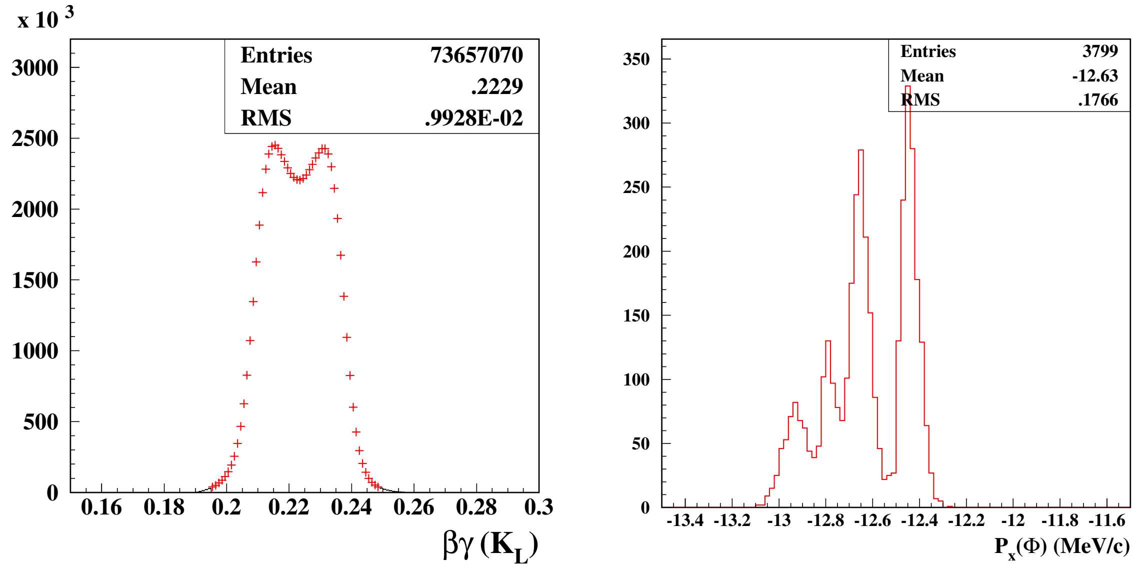

Figure 4: Left: $|p_{\vec{K}_L}|/m_K$ distribution of the K_L. Right: Momentum of the ϕ meson along the x-axis.

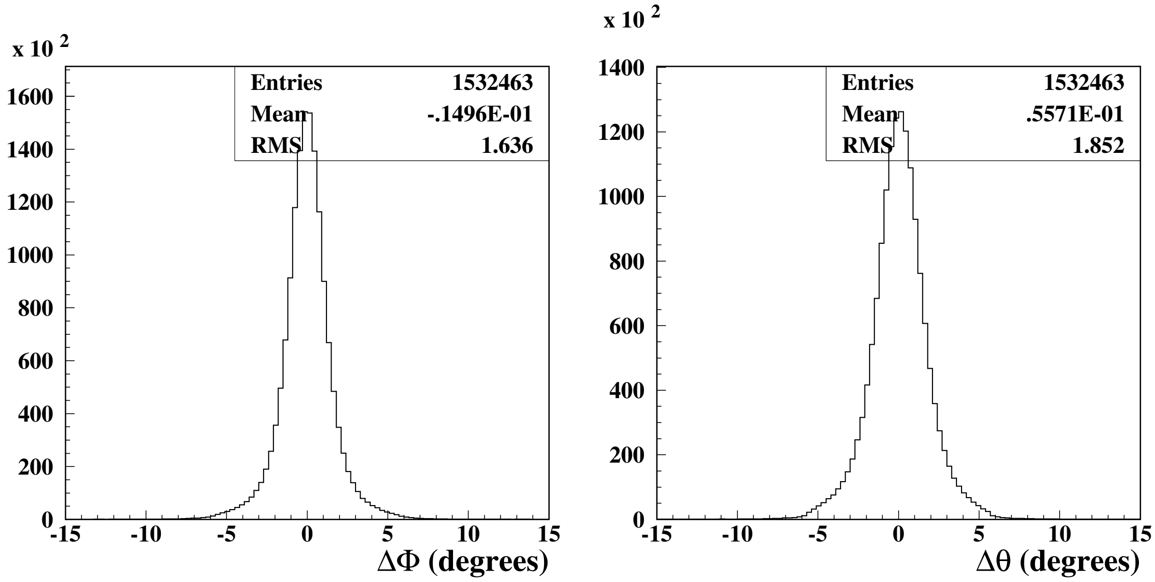

Figure 5: Resolution on the azimuthal ϕ and polar θ angles of the K_L flight direction obtained with $K_L \to \pi^+\pi^-\pi^0$ data.

3.1 Dependence of the tagging efficiency with L_K

$K_L \to \pi^0\pi^0\pi^0$ events are tagged by $K_S \to \pi^+\pi^-$ events which satisfy the requirements described in Section 3. The tagging efficiency has been evaluated by Monte Carlo as a function of L_K for the dominant K_L decay channels. For a K_L decaying in a given channel at a given L_K, we define the tagging efficiency as:

$$\epsilon(\text{tag}, K_L \to i, L_K) = \frac{N(\text{tag}, K_L \to i, L_K)}{N(K_L \to i, L_K)}$$

The results are shown in Fig. 6. The difference in tagging efficiency among the modes is mainly due to the dependence of the trigger efficiency on the K_L behaviour (Ref. [4]). Only the calorimeter trigger (Ref. [5]), which requires two local energy deposits above some threshold, is used for the present analysis. The trigger efficiency is, on average, $\sim$ 100 % for $K_L \rightarrow \pi^0\pi^0\pi^0$ and between $85 - 95\%$ for charged K_L decays. The trigger efficiency also depends on the position of the K_L decay vertex due to the use of position-dependent trigger thresholds. Another contribution is the dependence of the reconstruction efficiency for the pion tracks from $K_S \rightarrow \pi^+\pi^-$ on the presence of other tracks in the drift chamber. This contribution depends on the position of the K_L decay point and affects mainly events with $K_L \rightarrow$ charged particles near to the IP.

The tagging efficiency for the $K_L \rightarrow \pi^0\pi^0\pi^0$ channel has a linear dependence with L_K, with a slope almost compatible with zero, $b = (1.2 \pm 0.2) \times 10^{-5}$/cm, and an offset $a = (68.04 \pm 0.01)\%$ (Fig. 6).

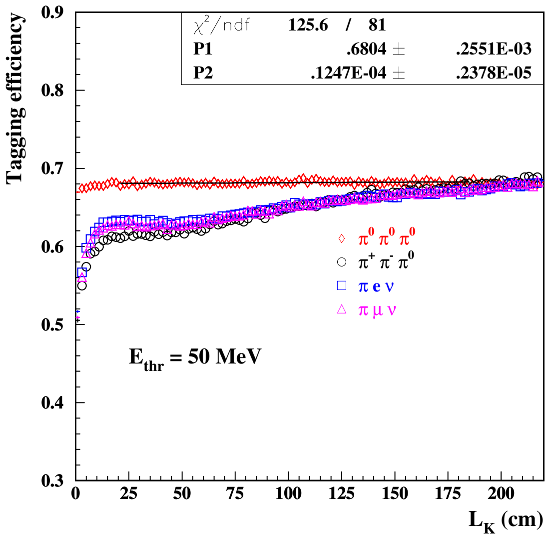

Figure 6: Tagging efficiency as a function of L_K for the main K_L decay channels.

4 Event preselection

The main characteristic of the $K_L \rightarrow \pi^0\pi^0\pi^0$ decay is to have a large number of photons. In order to minimize the effects due to the cluster reconstruction efficiency and acceptance corrections, we select K_L events with a number of clusters $N \geq 3$ on the calorimeter not associated to a track. Moreover, to reject low energy photons coming mainly from machine background, we require the clusters to have an energy $E \geq E_{thr}$, with E_{thr}=20 MeV. With this request the efficiency on the signal is, from Monte Carlo, $\sim (99.2 \pm 0.1)\%$. In Fig. 7 the energy distribution of a photon from $K_L \rightarrow \pi^0\pi^0\pi^0$ events is shown.

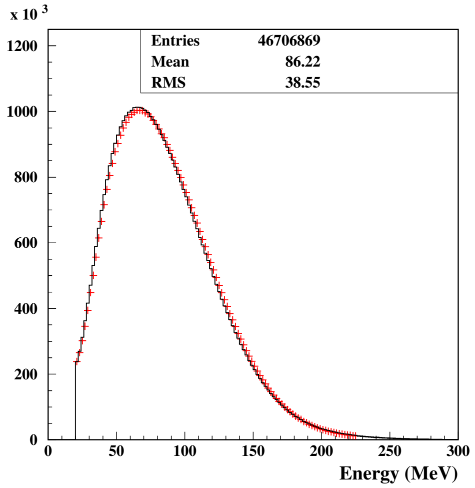

Figure 7: Energy distribution of each photon from $K_L \rightarrow \pi^0\pi^0\pi^0$ decay. Red crosses are data, solid histogram is Monte Carlo.

In order to reduce the contamination of $K_S \rightarrow \pi^0\pi^0$ events coming from regenerated K_S in the inner wall and external plates of the drift chamber, we select K_L with a polar angle with respect to the beam axis within $40° < \theta_L < 140°$. Since the angular distribution of $K_S K_L$ from a ϕ decay goes as $dN/d(\cos\theta) \propto \sin^2\theta$, the fraction of K_L inside this region is ~ 92.5 %.

The position of the K_L vertex is measured using K_L flight direction and the positions and arrival times of the photons on the calorimeter by solving the equations (Ref. [6]):

$$\begin{cases} L^2 + L_K^2 - 2LL_K\cos\theta & = L_\gamma^2 \\ L_K/\beta + L_\gamma & = ct_\gamma \end{cases}$$

Each photon determines the K_L decay length L_K up to a two-fold ambiguity, only one of the two solutions being geometrically correct. The resolution on the vertex as a function of the cluster energy goes as $\sigma(E) \sim a/\sqrt{E}$ (see Section 5.2).

The best estimate of L_K is taken as the energy-weighted average of the closest two L_{Ki} if they are not far away more than $5{\cdot}\sigma$ each other:

$$< L_K >= \frac{\sum_{i=1,2}(E_i \times L_{Ki})}{\sum_{i=1,2} E_i} \quad (2)$$

The Eq. 2 comes from the fact that the resolution on L_K as a function of the cluster energy goes as $\sigma(E) \sim a/\sqrt{(E)}$ (see Section 5.2).

The event is selected only if at least a third photon has a L_K within $5 \cdot \sigma$ with respect to the weighted average of the closest two.

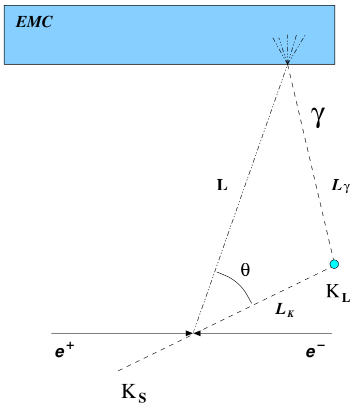

Figure 8: The time of flight triangle.

The decay vertex distribution for all detected photons after selection is shown in Fig. 9. No efficiency corrections or background subtraction have been applied at this stage. The two peaks clearly visible at short values of L_K are due to the $K_L \rightarrow K_S$ regeneration in the beam pipe and in the inner wall of the drift chamber. The vertex distributions obtained with a fixed number of photons are shown in Fig. 10: huge effects due to acceptance are clearly visible.

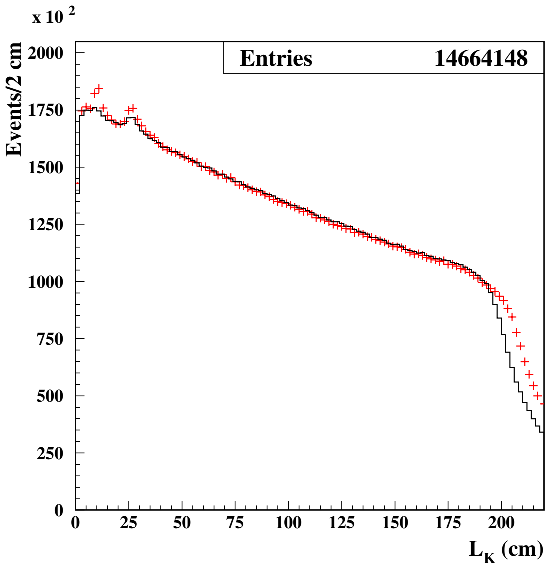

Figure 9: Decay length distribution for events with three or more than three neutral clusters connected to the same vertex. Red crosses are data, black histogram is Monte Carlo. The number of selected events is $\sim 14.7 \times 10^6$ for ~ 400 pb^{-1} integrated luminosity.

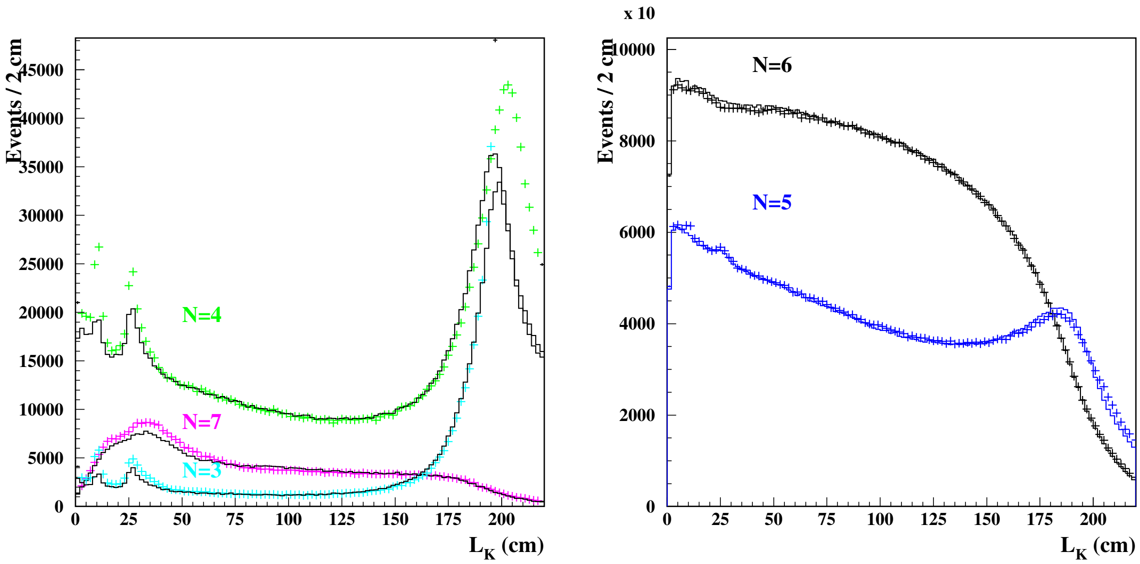

Figure 10: Decay length distribution for events with a fixed number of neutral clusters connected to the same vertex: N=3,4,7 (left) and N=5,6 (right). Crosses are data, solid histograms are Monte Carlo. For the $N = 3$ and $N = 4$ samples two peaks at the beam pipe and at the inner wall of the drift chamber are clearly visible due to the $K_L \to K_S$ regeneration with $K_S \to \pi^0\pi^0$.

5 Control sample

The $K_L \to \pi^+\pi^-\pi^0$ events are a good control sample because the kinematics is almost the same of $K_L \to \pi^0\pi^0\pi^0$ channel if we neglect the mass difference between neutral and charged pions. Moreover, in these events, the position of the K_L vertex is known from tracking and, therefore, it is possible to estimate:

1. the percentage of correct bunch-crossing identification;
2. the resolution on the K_L fligth direction;
3. the reliability of the algorithm for the reconstruction of the K_L decay vertex with photons;
4. the resolution on the decay vertex;
5. the time scale of the calorimeter;
6. the variation of the vertex reconstruction efficiency as a function of the decay path length.

5.1 Selection of $K_L \to \pi^+\pi^-\pi^0$ events

The selection of the $K_L \to \pi^+\pi^-\pi^0$ events has been performed without applying any cut related with the vertex position in order to avoid any possible biases in the determination of the quantities related to it. In the two tracks event sample we plot the distribution of the minimum $(|\vec{P}_{miss}| - E_{miss})$ value in the $\pi\mu$ or $\mu\pi$ hypothesys where:

$$\begin{aligned} \vec{P}_{miss} = &\quad \vec{P}_{K_L} - \vec{P}_1 - \vec{P}_2 \\ E_{miss} = &\quad E_{K_L} - E_{\vec{p1},\pi} - E_{\vec{p2},\mu} \text{ or } E_{K_L} - E_{\vec{p1},\mu} - E_{\vec{p2},\pi}. \end{aligned}$$

The distribution is shown in Fig. 11 (left). The peak centred at zero identifies $\pi\mu\nu$ events while $\pi^+\pi^-\pi^0$ and $\pi e\nu$ events are respectively in the negative and positive part of the spectrum. To select $\pi^+\pi^-\pi^0$ events we require $(|\vec{P}_{miss}| - E_{miss}) <$ -80 MeV. The momenta of the two selected tracks in the pion hypothesis are used to compute the π^0 mass, $m(\pi^0) = \sqrt{(E^2_{miss} - p^2_{miss})}$. The distribution is shown in Fig. 11 (right).

A second cut has been applied in order to identify the correct pair of photons coming from the π^0: the best pair has been selected as the one whose total energy $E_{\pi^0}(\gamma\gamma) = E(\gamma_1) + E(\gamma_2)$ best matches the expected pion energy estimated by the knowledge of the energies of the two charged pions and the energy of the K_L, E_{π^0}(expected) $= E(K_L) - E(\pi^+) - E(\pi^-)$. Only events that satisfy the requirement $|E_{\pi^0}(\gamma\gamma) - E_{\pi^0}(\text{expected})| <$ 40 MeV are selected (Fig. 12, left). At the end of the selection the background contamination is $\sim 2\%$ and the invariant mass built with the best pair of photons is peaked at the correct π^0 mass value (Fig. 12, right).

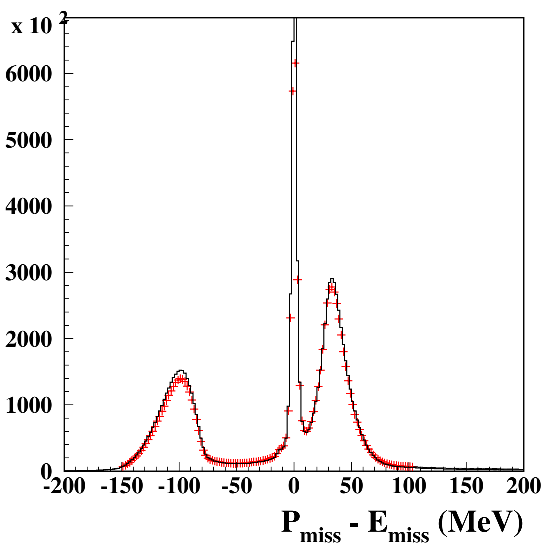

Figure 11: Selection of the control sample $K_L \to \pi^+\pi^-\pi^0$: $(|\vec{P}_{miss}| - E_{miss})$ distribution (left) and the missing mass distribution built from the charged pions and K_L (right). Red crosses are data, black histogram is Monte Carlo. The background contamination is shown as the small blue histogram.

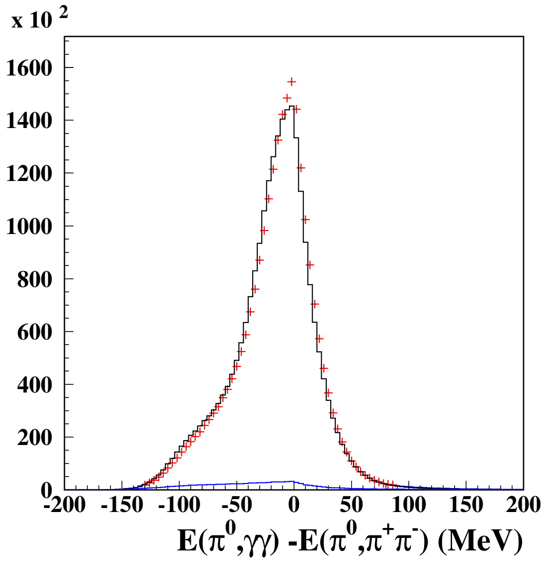

Figure 12: Selection of the control sample $K_L \to \pi^+\pi^-\pi^0$: $(E_{\pi^0}(\gamma\gamma) - E_{\pi^0}(\text{expected}))$ distribution (left) and invariant mass distributions of the best photon pair (right). Red crosses are data, black histogram is Monte Carlo. The background contamination is shown as the small blue histogram.

5.2 Vertex resolution

The vertex position is given by the energy-weighted average of the decay path lengths L_K of the two selected photons:

$$< L_K >= \frac{\sum_{i=1,2}(E_i \times L_{Ki})}{\sum_{i=1,2} E_i} \tag{3}$$

where this formula holds because the vertex resolution as a function of the energy goes as $\sigma \sim a/\sqrt{E}$ (see below, Fig. 13).

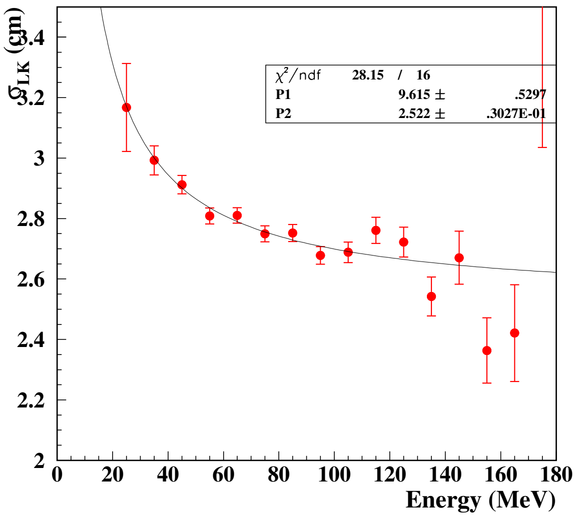

Figure 13: $L_K(\pi^+\pi^-) - L_K(\gamma)$ distribution obtained with $\pi^+\pi^-\pi^0$ events as a function of the energy of one of the two photons.

Moreover a dependence of the resolution from the decay path length L_K is also expected due to the finite angular resolution on the K_L flight direction (see Fig. 5).

The vertex resolution function has been studied by comparing the position of the vertex reconstructed by the photons, $L_K(\gamma\gamma)$, with the one reconstructed by the two pions tracks, $L_K(\pi^+\pi^-)$. Given the excellent vertex resolution measured in the drift chamber ($\sim$ 1 mm), the width of the distribution of the difference $(L_K(\pi^+\pi^-) - L_K(\gamma\gamma))$ is dominated by the resolution on the $L_K(\gamma\gamma)$.

An example of the $L_K(\pi^+\pi^-) - L_K(\gamma\gamma)$ distribution integrated over all the energies and over the fiducial volume is shown in Fig. 14.

Two different fits have been performed: a single-gaussian fit and a double-gaussian fit.

In the case of a double gaussian function, the relative weights of the two gaussians are left free parameters of the fit.

In the case of a fit with a single gaussian (χ^2/ndf = 1085/292) the σ_0 = 2.5 cm. In the case of the double-gaussian fit (χ^2/ndf= 395/289) the bulk of the distribution ($\sim$ 82% of the total) has σ_1 = 2.1 cm while the tails are described by a broader gaussian ($\sim$ 18% of the total) with σ_2 = 5.4 cm.

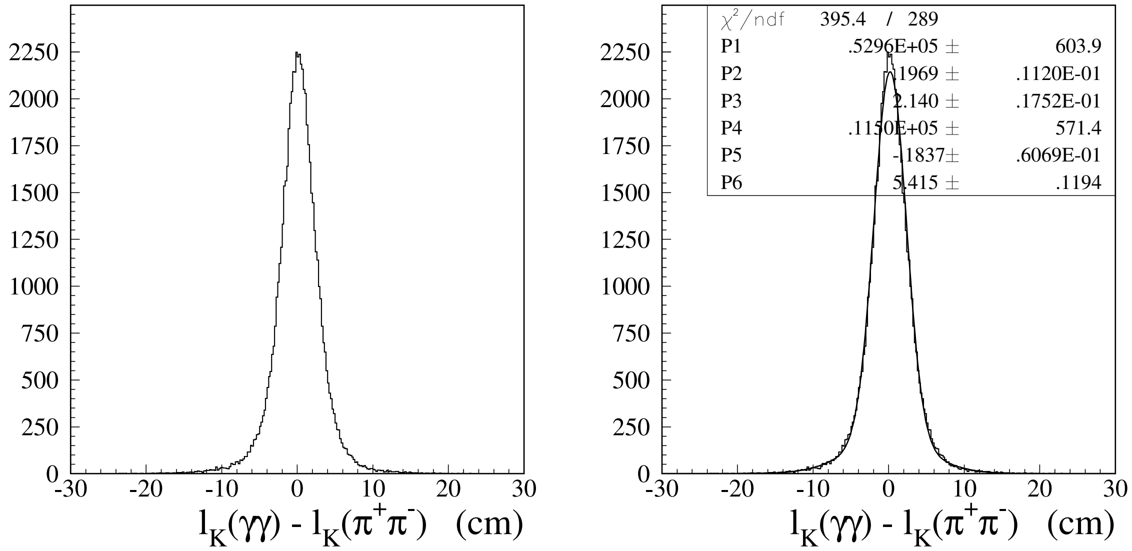

Figure 14: $L_K(\pi^+\pi^-) - L_K(\gamma\gamma)$ distribution obtained with $\pi^+\pi^-\pi^0$ events. The two-gaussians fit is shown to the right.

The same fits have been repeated by dividing the FV in subregions 10 cm wide in L_K. The dependence of σ_0 with L_K is shown in Fig. 15. The resolution has a quadratic dependence on L_K and ranges from 2 cm at $L_K \sim 0$ cm to $\sim$ 4 cm at the boundary of the decay volume.

The dependence of σ_1 and σ_2 and of the relative weights of the two gaussians with L_K is shown in Fig. 16. Both σ_1 and σ_2 have a quadratic dependence with L_K: in the FV (between 40 and 165 cm) $\sigma_1(L_K)$ ranges from 1.5 cm to 3 cm while the weight of the corresponding gaussian goes from 82% to 65%. $\sigma_2(L_K)$ goes from 4.5 cm to 5.5 cm while its weight increases from 18% to 35 %. Since for each point the weighted-average of σ_1 and σ_2 agrees at 10% level with the σ of a single-gaussian fit, we use the latter as estimate of the vertex resolution. The effect of the tails on the fit value are discussed in Section 9.2 .

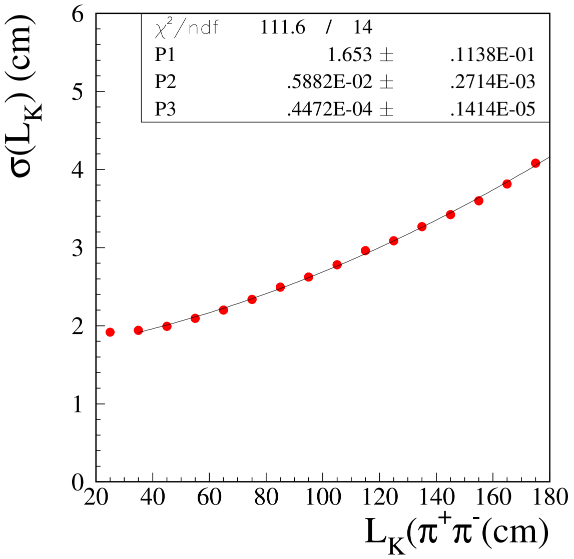

Figure 15: Vertex resolution as a function of L_K for $\pi^+\pi^-\pi^0$ events in the case of a single gaussian fit.

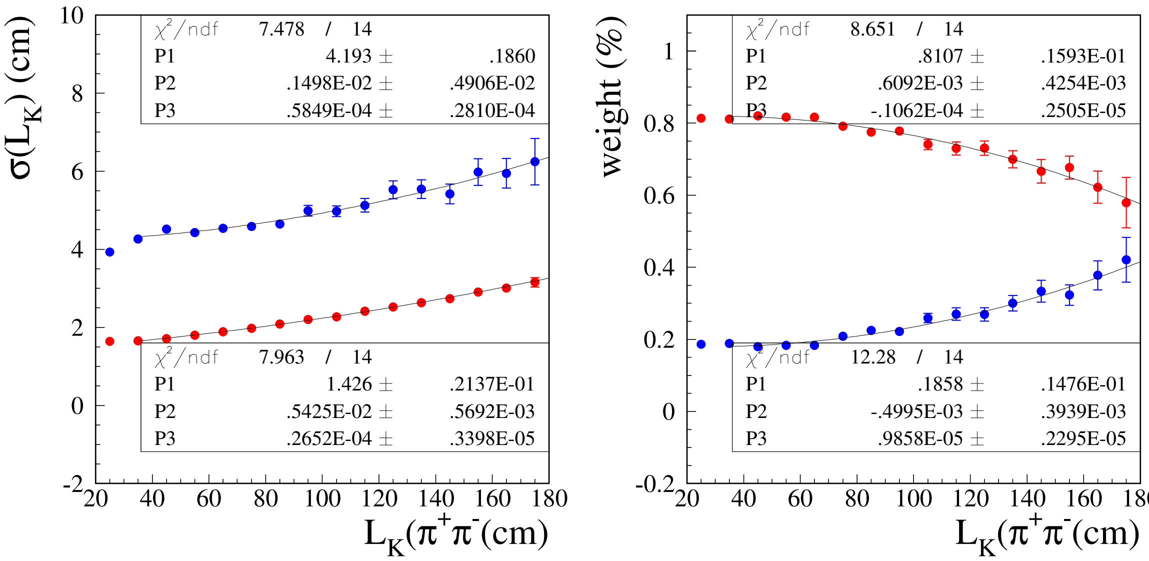

Figure 16: Double gaussians fit: vertex resolutions σ_1 and σ_2 (left) and relative weights of the two gaussians (right) as a function of L_K for $K_L \to \pi^+\pi^-\pi^0$ events.

5.3 Absolute time scale of the calorimeter

The value of the average of the $L_K(\pi^+\pi^-) - L_K(\gamma\gamma)$ distribution as a function of $L_K(\pi^+\pi^-)$ position is used to check the absolute time calibration of the calorimeter. The analysis has been carried out on the whole data sample and the result is shown in Fig. 17. The vertex reconstructed by the calorimeter has on average an offset of 2 mm and a slope compatible with zero with respect to the vertex reconstructed by the drift chamber. This analysis has been repeated over 21 groups of runs of $\sim$ 20 pb^{-1} each. The output of this analysis shows that the data sample consists of two samples of runs: the first ($\sim$ 65 pb^{-1}, first period of 2001 data taking) which has a parabolic dependence on L_K starting from 2 mm and decreasing up to -0.4 mm at the end of the decay volume (Fig. 18, left). The second ($\sim$ 335 pb^{-1}) which has also a parabolic dependence with L_K and increases from 2 mm at $L_K \sim 20$ cm to 3 mm at $L_K \sim 170$ cm (Fig. 18, right). The two effects tend to compensate when the runs are summed up together.

The origin of these miscalibrations is due to the fact that the time calibration procedure for the two groups of runs was slightly different, in particular as far as concern the definition of the bunch-crossing period T: for the first group was directly measured on data using $e^+e^- \to \gamma\gamma$ events, for the second group was forced to be equal to the radio-frequency period of the DAΦNE machine.

These miscalibrations have a negligible effect on the lifetime measurement. However they are taken into account by correcting the reconstructed decay path L_K event by event for the observed dependencies. The systematic error associated to this correction is discussed in Section 9.3.

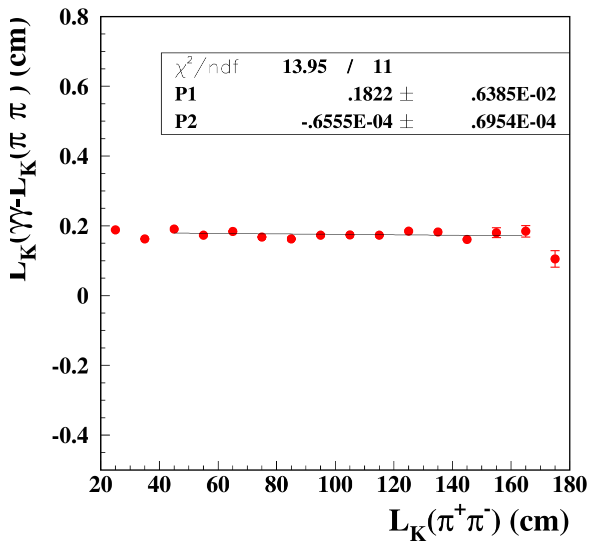

Figure 17: Difference of the K_L vertex position reconstructed by the calorimeter ($L_K(\gamma\gamma)$) with respect to the one reconstructed by the drift chamber ($L_K(\pi^+\pi^-)$) as a function of $L_K(\pi^+\pi^-)$ in $K_L \to \pi^+\pi^-\pi^0$ events for the full data sample.

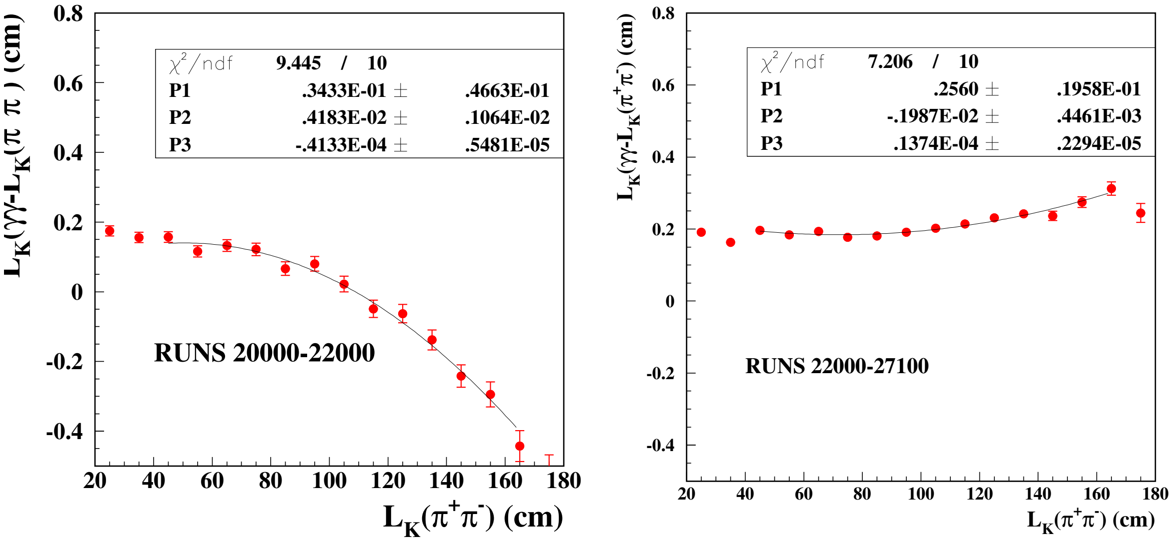

Figure 18: Difference of the K_L vertex position reconstructed by the calorimeter ($L_K(\gamma\gamma)$) with respect to the one reconstructed by the drift chamber ($L_K(\pi\pi)$) as a function of $L_K(\pi\pi)$ in $K_L \to \pi^+\pi^-\pi^0$ events for two different group of runs: the first corresponds to ~ 65 pb^{-1} (left) and the second to ~ 335 pb^{-1} (right) of integrated luminosity.

5.4 Vertex reconstruction efficiency

The position of the decay vertex of the K_L is given by the energy-weighted average of the two closest vertices obtained with the time of flight algorithm from photons belonging to the same event. The two closest vertices are kept only if they are within a time window of $5{\cdot}\sigma$ each other. The σ depends on the K_L path length L_K as (Fig. 15):

$$\sigma(L_K) = (1.65 + 0.59 \cdot 10^{-2}/\text{cm} L_K + 0.45 \cdot 10^{-4}/\text{cm}^2 L_K^2)\ \text{cm}$$

For lifetime measurement it is crucial to keep under control the variation of the vertex reconstruction efficiency with L_K. For the $K_L \to \pi^0\pi^0\pi^0$ events, the only way to do it is using Monte Carlo where the true position of the vertex is known.

For the $\pi^0\pi^0\pi^0$ sample the vertex is reconstructed at the beginning of the selection by counting the number of events (N_γ) with at least three photons with $E \geq 20$ MeV and, among them, the number of events with a vertex reconstructed within a time window of $5{\cdot}\sigma$ with respect to the true one (N_v). We compute the vertex reconstruction efficiency as a function of L_K. For each bin i in L_K (1 bin = 2 cm) we have:

$$\epsilon(i) = \frac{N_\gamma(i)}{N_t(i)} \times \frac{N_v(i)}{N_\gamma(i)}$$

where N_t is the number of events that have a *true* (MC) vertex in that bin.

The result obtained by Monte Carlo for $K_L \to \pi^0\pi^0\pi^0$ events is shown in Fig. 19. In the range 40 cm $< L_K <$ 165 cm the efficiency is ~ 99.2 % with a linear dependence on the vertex position of $\sim -2 \cdot 10^{-5}$/cm.

In order to study this dependence on data, we use the $K_L \to \pi^+\pi^-\pi^0$ sample where the position of the vertex is known by tracking with the drift chamber. In this case the vertex is reconstructed at the end of the $\pi^+\pi^-\pi^0$ selection where the presence of two photons is assumed (see Section 5.1). The efficiency for each bin is therefore defined as:

$$\epsilon(i) = \frac{N_v(i)}{N_t(i)}$$

The results both for data and Monte Carlo are shown in Fig. 20 (left). In Fig. 20 (right) we show the ratio of the two curves. The results obtained with $K_L \to \pi^0\pi^0\pi^0$ and $K_L \to \pi^+\pi^-\pi^0$ samples show that:

1. the absolute value of the vertex efficiency is different as a consequence of the fact that the two closest vertices are chosen in a sample with more than three photons for $K_L \to \pi^0\pi^0\pi^0$ events and in a sample with just two photons for $K_L \to \pi^+\pi^-\pi^0$ events. Moreover the vertex efficiency in the $\pi^0\pi^0\pi^0$ sample takes also into account the probability of finding at least three neutral clusters with $E \geq 20$ MeV.

2. There is a wide region (from 30 cm to 165 cm) in which the efficiency has a linear behaviour with a negative slope of $\sim -2 \cdot 10^{-5}$/cm;

3. All the slopes are compatible within the errors.

The fact that the slopes are equal means that the lost of events in the $\pi^0\pi^0\pi^0$ sample due to the request to have at least three photons with $E \geq 20$ MeV is uniform in the fiducial volume at the level of the statistical accuracy.

The K_L decay length distribution (Fig. 9) is corrected bin by bin with the efficiency values obtained from the $K_L \rightarrow \pi^0\pi^0\pi^0$ Monte Carlo sample multiplied by the data Monte Carlo efficiency ratio obtained from $K_L \rightarrow \pi^+\pi^-\pi^0$ events (Fig. 20):

$$\epsilon(\pi^0\pi^0\pi^0\,,\text{data}) = \epsilon(\pi^0\pi^0\pi^0\,,\text{MC}) \times \frac{\epsilon(\pi^+\pi^-\pi^0\,,\text{data})}{\epsilon(\pi^+\pi^-\pi^0\,,\text{MC})} \quad (4)$$

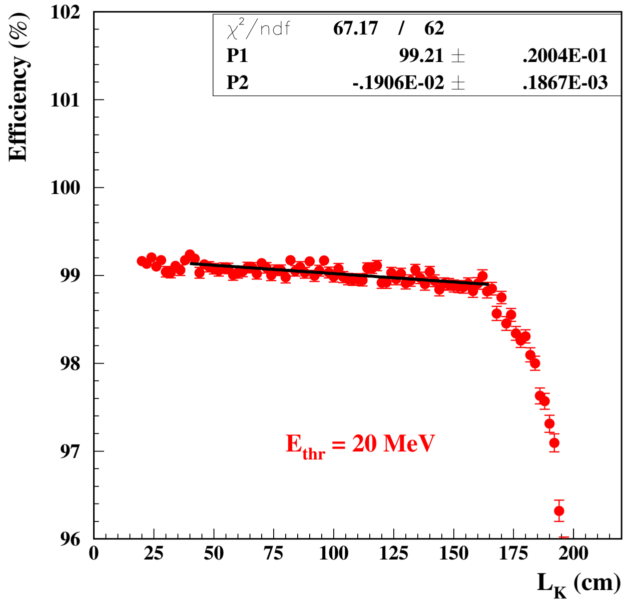

Figure 19: Variation of the vertex reconstruction efficiency with the decay path length for $K_L \rightarrow \pi^0\pi^0\pi^0$ Monte Carlo events.

In order to check the robustness of this procedure we changed the width of the acceptance window from $5 \cdot \sigma$ to $10 \cdot \sigma$. The results obtained for 5,6,7 and 10 σ are shown in Fig. 21

All the slopes are equal within 5 % while their statistical error goes from 16 % for $TW = 10 \cdot \sigma$ to 37 % for $TW = 5 \cdot \sigma$.

The only effect of the increasing the window is to change the efficiency value, or, in other words, to increase the number of events reconstructed with a good vertex. The efficiency values for different acceptance windows are plugged bin by bin into the proper time distribution and the fit has been repeated. The results of the fit are equal within their statistical accuracy.

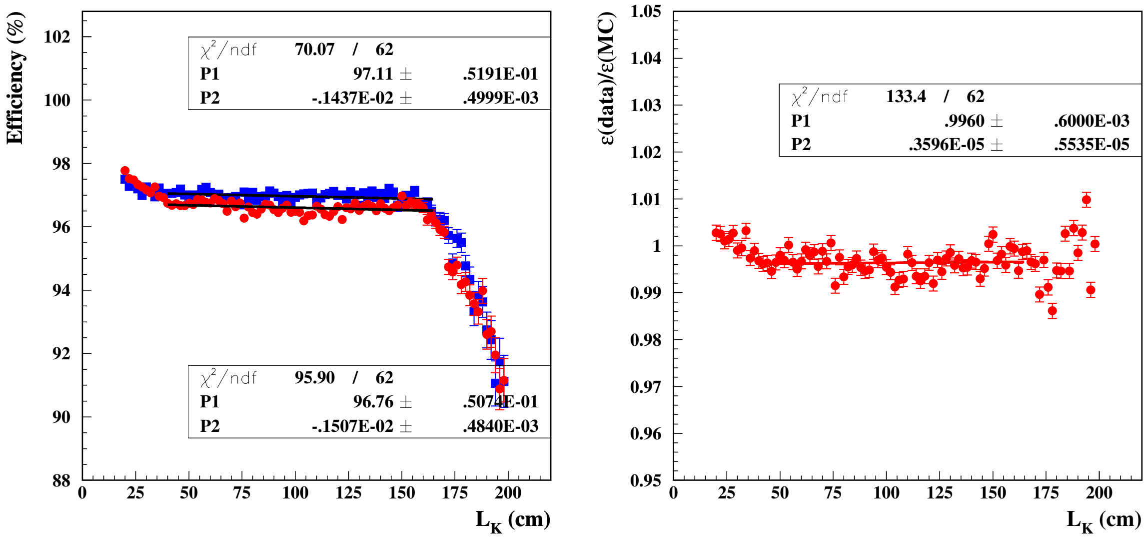

Figure 20: Left: variation of the vertex reconstruction efficiency with the decay path length for $K_L \to \pi^+\pi^-\pi^0$ data (red dots) and Monte Carlo (blue squares) events. Right: ratio of the two curves.

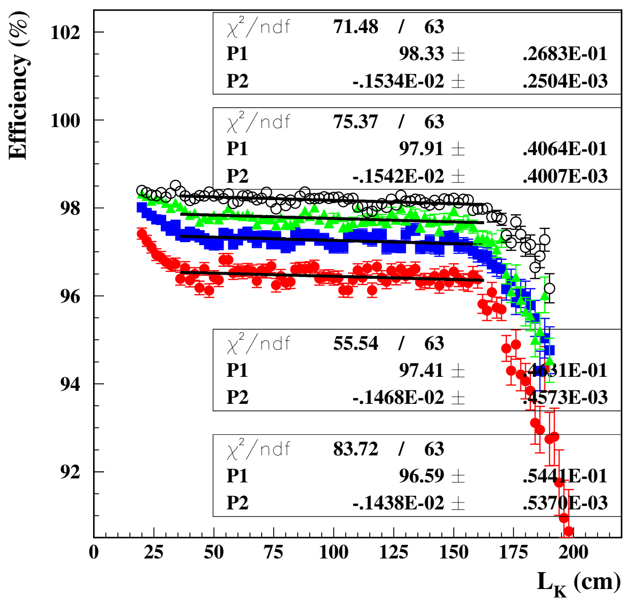

Figure 21: Variation of the reconstruction efficiency of the K_L vertex with the decay path length for $K_L \to \pi^+\pi^-\pi^0$ data events as a function of the acceptance window around the vertex reconstructed with the drift chamber. Black empty circles are for $10 \cdot \sigma$, green triangles for $7 \cdot \sigma$, blues squares for $6 \cdot \sigma$ and red circles for $5 \cdot \sigma$ around the vertex reconstructed with the drift chamber.

6 Signal selection and background contamination

The background contamination is concentrated in the event samples with three ($N = 3$) and four ($N = 4$) photons associated to the vertex, while the events with more than four photons are almost background free. The $N = 3$ and $N = 4$ samples are, from Monte Carlo, respectively the $\sim 1.1\%$ and 7.7% of the total number of events. The dominant sources of backgrounds are:

1. $K_L \rightarrow \pi^+\pi^-\pi^0$ events where the K_L decays close to the calorimeter and the two charged pions have either one or none reconstructed track or a track not associated to a cluster;
2. the CP-violating decay $K_L \rightarrow \pi^0\pi^0$;
3. the decay $K_S \rightarrow \pi^0\pi^0$ where the K_S is regenerated either in the beam pipe or in the inner wall of the drift chamber or in the drift chamber itself.

In Fig. 22 and Fig. 23 the various background components are shown as a function of the decay vertex for $N = 3$ and $N = 4$ samples before the selection cuts. For the $N = 3$ sample we show also the total energy distribution (defined as the sum of the photon energies for each event). The huge amount of background coming from $K_L \rightarrow \pi^+\pi^-\pi^0$ events is clearly visible especially at high values of L_K, where the tracking efficiency is lower.

In Table 1 we show the background components which survive the preselection cuts (see Section 4) in the fiducial volume (FV) defined as:

$$40 \text{ cm} < L_K < 165 \text{ cm} \tag{5}$$
$$40^\circ < \theta_L < 140^\circ \tag{6}$$

In the evaluation of these numbers we use the full Monte Carlo sample (~ 500 pb^{-1}). The $N = 3$ and $N = 4$ event samples are examined in details. The total background contamination $k = B/(S + B)$ is $\sim 4.9\%$ among which $\sim 4.1\%$ affects the $N = 3$ sample (mainly due to $\pi^+\pi^-\pi^0$ events with splitted clusters or clusters not associated to tracks) and $\sim 0.7\%$ affects the $N = 4$ sample (mainly due to $K_L \rightarrow \pi^0\pi^0$ and $K_L \rightarrow K_S \rightarrow \pi^0\pi^0$ events).

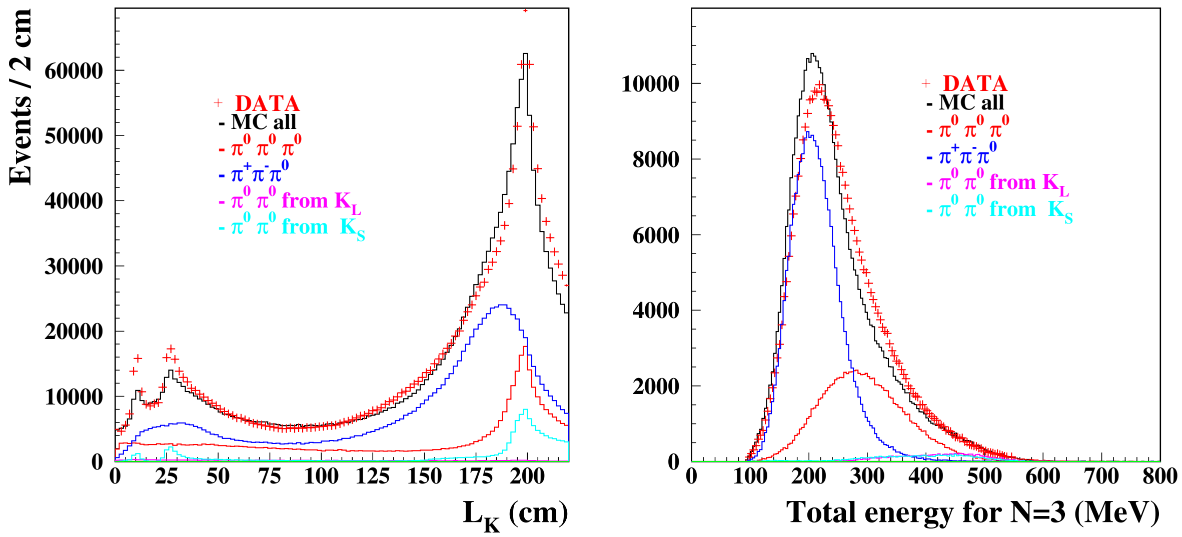

Figure 22: Decay vertex distribution (left) and total energy distribution (right) for the $N = 3$ sample. Red points are data, black line is Monte Carlo (signal+background). The contributions from different channels are shown as coloured histograms.

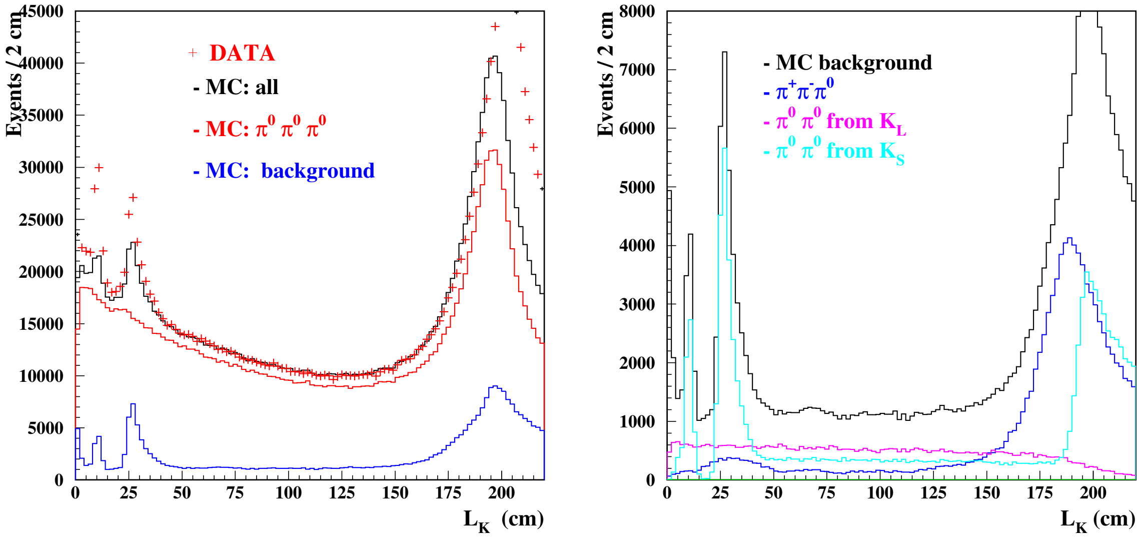

Figure 23: Left: decay vertex distribution for $N = 4$ selected photons. Red points are data, black line is Monte Carlo (signal + background). Right: zoom of the Monte Carlo background distribution. The contributions of different channels are shown as coloured histograms.

	N≥3		N=3		N=4	
K_L channel	events	B/(S+B)	events	B/(S+B)	events	B/(S+B)
signal+backgrounds	10536674		535725	–	726084	–
signal	10018154	-	99063	–	649234	–
all backgrounds	518520	4.92 %	436662	4.14 %	76850	0.73 %
$K_L \rightarrow \pi^+\pi^-\pi^0$	325076	3.08 %	308984	2.93 %	15074	0.14 %
$K_L \rightarrow \pi\mu\nu$	28917	0.28 %	26658	0.25 %	2082	0.02 %
$K_L \rightarrow \pi e\nu$	49140	0.47 %	45513	0.43 %	3355	0.03 %
$K_L \rightarrow \pi^0\pi^0$	43436	0.41 %	9826	0.1 %	32003	0.30 %
$K_L \rightarrow K_S \rightarrow \pi^0\pi^0$	30273	0.29 %	8241	0.09 %	20901	0.20 %
$K_L \rightarrow other$	41298	0.39 %	37101	0.35 %	3398	-

Table 1: Event types in the FV for $N \geq 3$, $N = 3$ and $N = 4$ photons connected to the same vertex. The background contamination $(B/(S+B))$ in the same fiducial volume is also shown.

To reject the background in the $N = 3$ sample we require at least one cluster on the barrel with at least 50 MeV energy and no tracks with a distance of closest approach (DCA) to the K_L line of flight less than 20 cm. The DCA distribution is shown in Fig. 24 (left). In Fig. 24 (right), we show the $N = 3$ signal efficiency (red circles) and the signal to background ratio (blue squares) as a function of the cut on DCA. The efficiency has been studied with Monte Carlo as a function of L_K: we find an almost flat dependence in the FV with an average value of $\sim 55\%$ (Fig. 25). The effect of this cut on the measurement of the K_L lifetime will be discussed later.

No cuts are applied for events with four detected photons.

In Table 2 we show the percentages of the background components before and after the selection cuts. The background contamination is reduced from $\sim 4.9\%$ to $\sim 1.3\%$ with an efficiency on the signal of $\sim 99.6\%$. The distributions of the total energy for events with $N = 3, 4, 5, 6, 7, \geq 8$ photons are shown in Fig. 27. For $N = 3$ and $N = 4$ event samples the different contributions from the residual background components are also shown.

After the selection cuts we compare in data and Monte Carlo the relative weight of events with $N = 3, 4, 5, 6, 7, \geq 8$ in the fiducial volume. The results are shown in Fig. 28 and in Table 3. The few percent differences between data and Monte Carlo are mainly due to a higher amount of splitted clusters in Monte Carlo than in data[4].

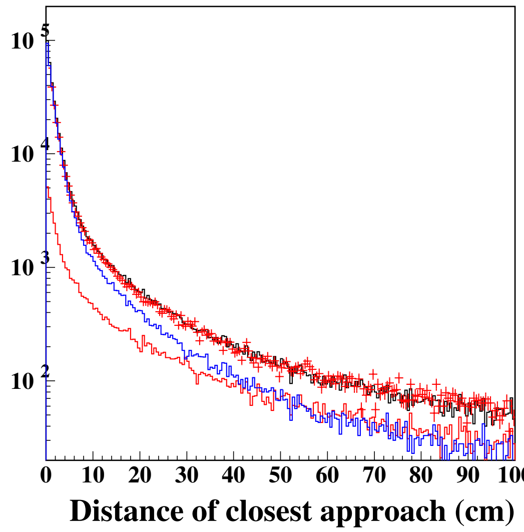

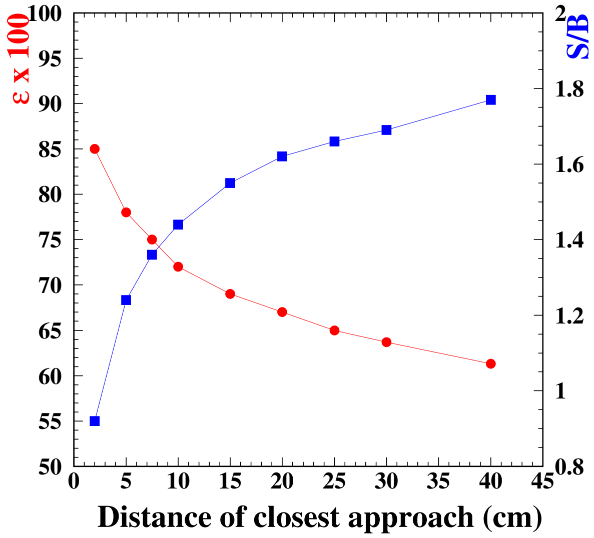

Figure 24: Left: distance of closest approach of a track to the K_L line of flight. Red dots are data, solid histograms Monte Carlo: the black histogram is signal+background, the red histogram is signal and the blue histogram is background. Right: efficiency (red circles) and signal to background ratio (blue squares) for different cuts on the distance of closest approach.

[4]The different amount of splitted clusters between data and Monte Carlo is due to the fact that in the Monte Carlo we have an effective threshold for each calorimeter channel of ~ 1 photoelectron, while in the data is 4-5 times bigger.

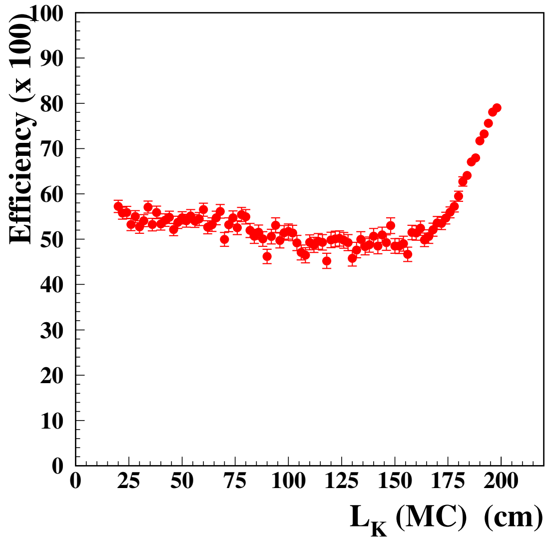

Figure 25: Efficiency (from Monte Carlo) for the selection cuts on the $N = 3$ events as a function of the K_L decay path.

	N≥3 BEFORE cuts		N≥3 AFTER cuts	
K_L channel	Events	B/(S+B)	Events	B/(S+B)
signal+backgrounds	10536674		10114899	
all backgrounds	518520	4.92 %	133535	1.32 %
$K_L \rightarrow \pi^+\pi^-\pi^0$	325076	3.08 %	44917	0.44 %
$K_L \rightarrow \pi\mu\nu$	28917	0.28 %	3583	0.03 %
$K_L \rightarrow \pi e\nu$	49140	0.47 %	6062	0.06 %
$K_L \rightarrow \pi^0\pi^0$	43436	0.41 %	42313	0.42 %
$K_L \rightarrow K_S \rightarrow \pi^0\pi^0$	30273	0.29 %	28166	0.28 %
$K_L \rightarrow$ *other*	41298	0.39 %	8440	0.08 %

Table 2: Event types in the fiducial volume from Monte Carlo before and after the selection cuts. The background contamination $k = B/(S + B)$ is also shown.

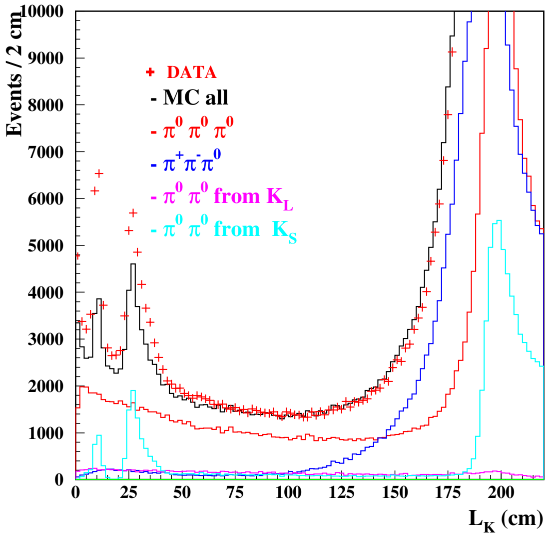

Figure 26: Decay vertex distributions for $N = 3$ after the selection cuts. Red crosses are data, black line is Monte Carlo (signal + background). The contributions from different channels are shown as coloured histograms.

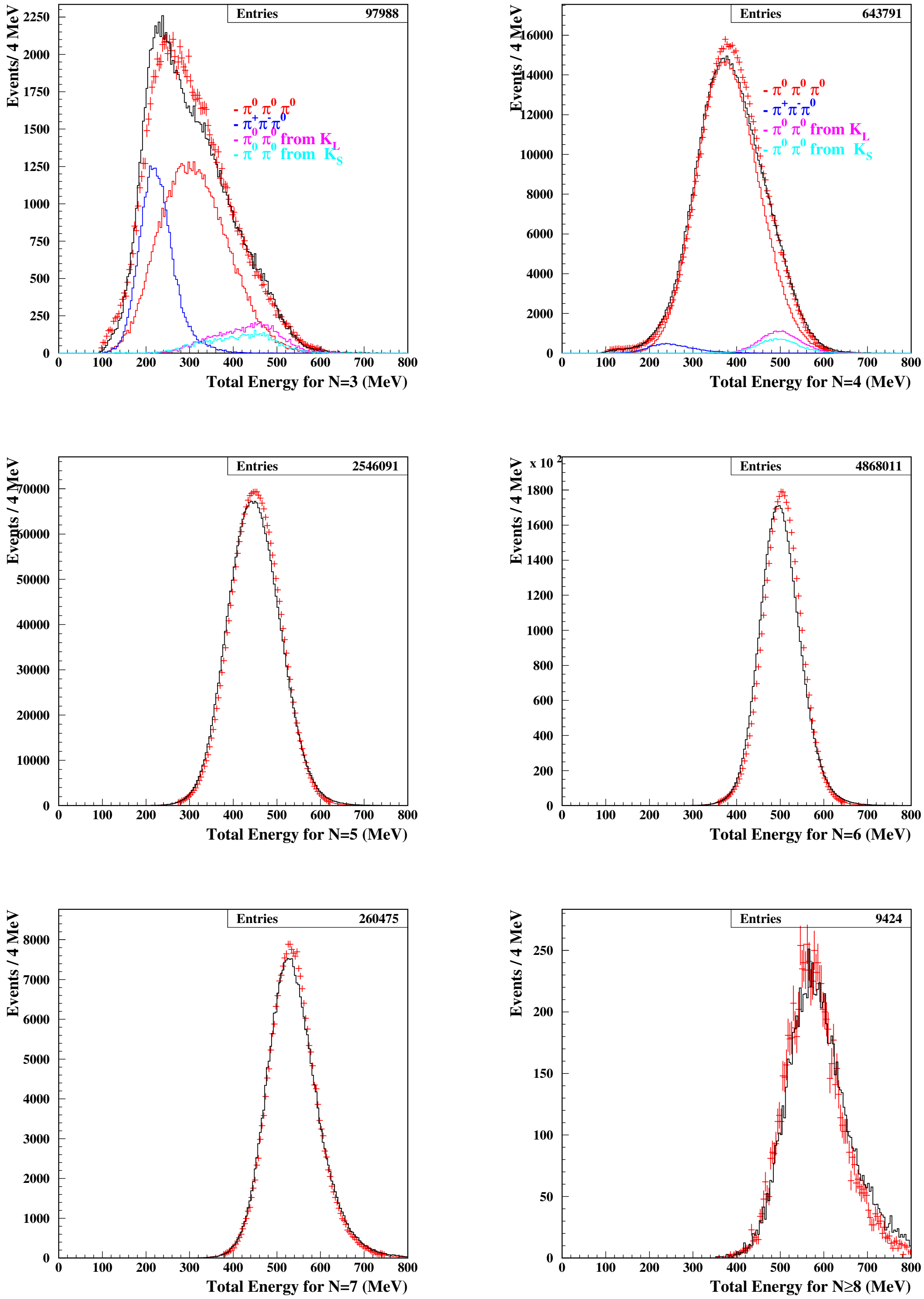

Figure 27: Total energy distributions for events with $N = 3, 4, 5, 6, 7, \geq 8$ photons in the fiducial volume. Red crosses are data, black histograms are Monte Carlo. For the samples with $N = 3$ and $N = 4$ photons, the contributions from the residual background components are also shown.

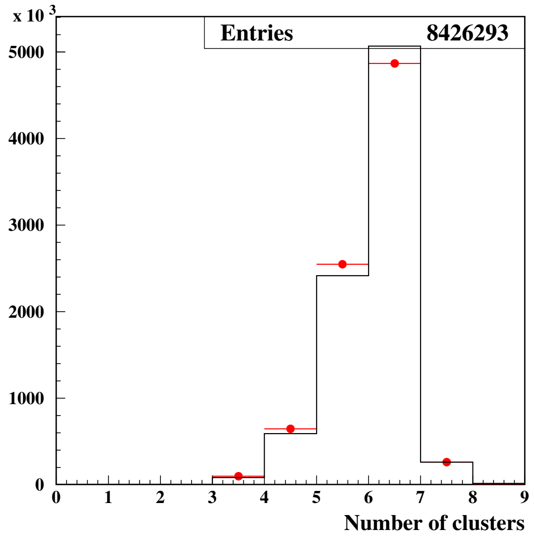

Figure 28: Cluster multeplicities in the fiducial volume. Red dots are data, solid histogram is Monte Carlo.

Number of clusters	Data	Monte Carlo
3	1.163 $\pm$ 0.004 %	0.980 $\pm$ 0.003 %
4	7.64 $\pm$ 0.01 %	7.01 $\pm$ 0.01 %
5	30.22 $\pm$ 0.02 %	28.65 $\pm$ 0.02 %
6	57.77 $\pm$ 0.03 %	60.12 $\pm$ 0.03 %
7	3.091 $\pm$ 0.006 %	3.074 $\pm$ 0.001 %
≥ 8	0.106 $\pm$ 0.001 %	0.151 $\pm$ 0.001 %

Table 3: Relative weight of cluster multeplicities in fiducial volume.

7 Effect of K_L nuclear interactions

K_L nuclear interactions with the material inside the drift chamber bias the lifetime measurement since they modify the rate of decaying K_L's. In fact, the decrease in the number of K_L passing from L to $L + dL$ is given by:

$$N(L + dL) - N(L) = -N(L) \cdot (\frac{1}{\lambda_L} + \frac{1}{\lambda_I}) \cdot dL$$

or:

$$N(L) = N(0) \cdot e^{-L/\lambda_{exp}}$$

where:

$$\lambda_{exp} = \frac{\lambda_I \lambda_L}{(\lambda_I + \lambda_L)} \simeq \lambda_L (1 - \frac{\lambda_L}{\lambda_I}) \qquad (7)$$

and λ_L is the K_L mean path length, $\lambda_I = 1/(N_A \cdot \rho(L) \cdot \sigma_I)$ and N_A is the Avogadro number, $\rho(L)$ the material density and σ_I the nuclear interaction cross section. The dominant nuclear interaction processes, $K_L \rightarrow K_S$ regeneration, $\overline{K}^0 N \rightarrow \Sigma\pi$ and $\overline{K}^0 N \rightarrow \Lambda\pi$ are simulated in the Monte Carlo. From Gheisha, λ_I in the drift chamber material is ~ 50000 cm while $\lambda_L \sim 340$ cm in KLOE. Therefore, from Eq. 7, we expect to find a λ_L reduced by a factor $\lambda_L/\lambda_I \sim 0.7\%$ with respect to the true value. Actually, if we plot the distribution of the *true* Monte Carlo decay vertices of K_L's without applying any tagging or selection and we fit it with an exponential function, we find out $\tau_L \sim (51.35 \pm 0.13)$ ns, i.e. $\sim 0.67\%$ lower than the GEANT value ($\tau_L = 51.7$ ns), as expected.

The rates for all three types of interaction processes are also determined using data (Ref. [4]) and the simulation is corrected accordingly. In data the sum of all the nuclear interactions amounts to $\sim 0.33\%$ with a conservative error of 50%, $(0.33 \pm 0.16)\%$. This value has been taken into account to correct the K_L lifetime.

8 Fit of the proper time distribution

The K_L proper time, t^*, is obtained event by event dividing the decay length L_K by the $\beta\gamma$ of the K_L in the laboratory, $t^* = L_K/(\beta\gamma c)$ (Fig. 4).

In Fig. 29 we show the t^* distribution obtained with $\sim 14.7\times10^6$ $K_L\to\pi^0\pi^0\pi^0$ events after the background rejection cuts discussed in Section 6. The residual $\sim 1.3\%$ background is subtracted bin by bin using Monte Carlo predictions.

The relative variations of the vertex reconstruction efficiency as a function of the decay path length are taken into account by correcting bin by bin the decay vertex distribution with the values obtained with the $K_L \to \pi^0\pi^0\pi^0$ Monte Carlo sample multiplied by the data - Monte Carlo ratio of the efficiencies evaluated with $\pi^+\pi^-\pi^0$ sample (see Eq. 4).

The statistical uncertainty of the efficiency values (of the order of $\sim 0.1\%$) has been taken into account by adding it in quadrature to the statistical fluctuation of the entries in each bin after the background subtraction.

The distribution is fitted with an exponential function in the fiducial volume (see Eq. 6), which, in terms of proper time, ranges from 6 ns to 24.8 ns. With $\sim 8.5\cdot10^6$ events in the fit region we obtain:

$$\tau = (50.87 \pm 0.17_{\text{stat}})\ \text{ns}$$

with a $\chi^2 = 58$ for 62 degrees of freedom.

In the Appendix A we report all the relevant numbers necessary to compute the lifetime histogram.

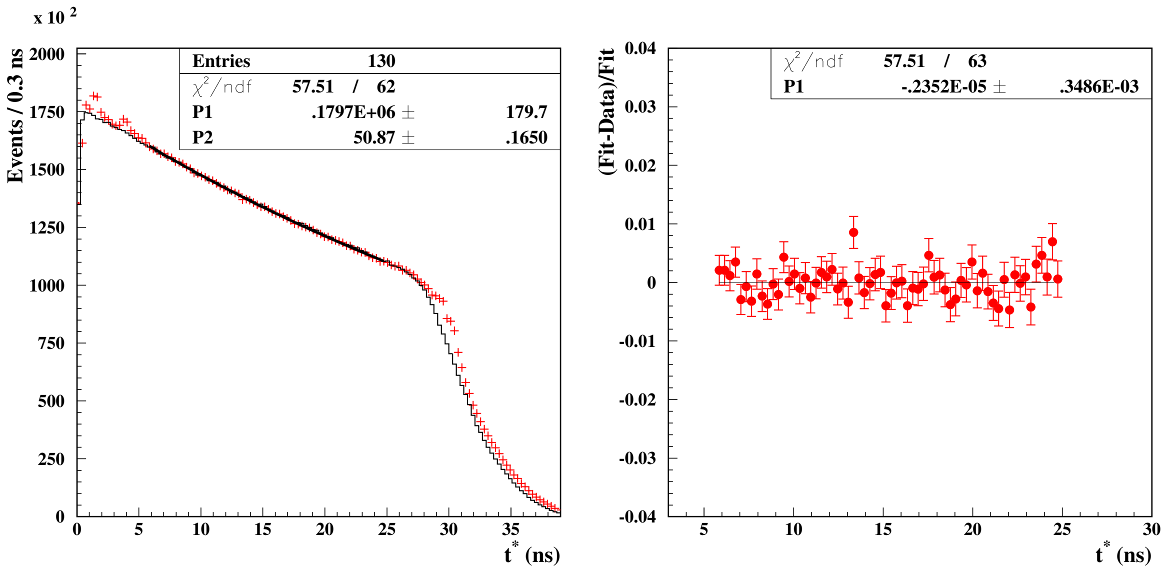

Figure 29: Fit of the proper time distribution. The residuals of the fit are shown to the left.

As already discussed (see Section 1), the statistical error on the lifetime measurement depends on the number of events, $\propto 1/\sqrt{N}$ and, very strongly, on the time interval covered (see Eq. 1).

We studied the dependence of the statistical error on the lifetime as a function of T by varying the lower limit of the fit from 4.8 ns to 12 ns with the upper limit fixed and the upper limit from 21 ns and 29.4 ns with the lower limit fixed. The results are shown in Fig. 30, blue circles. In the same plot (red squares) we show the prediction from Eq. 1 where N is the number of events after background subtraction and efficiency correction. The difference between the two curves is due to the statistical uncertainty of the vertex reconstruction efficiency values evaluated from Monte Carlo that has been added in quadrature bin by bin to the proper time distribution.

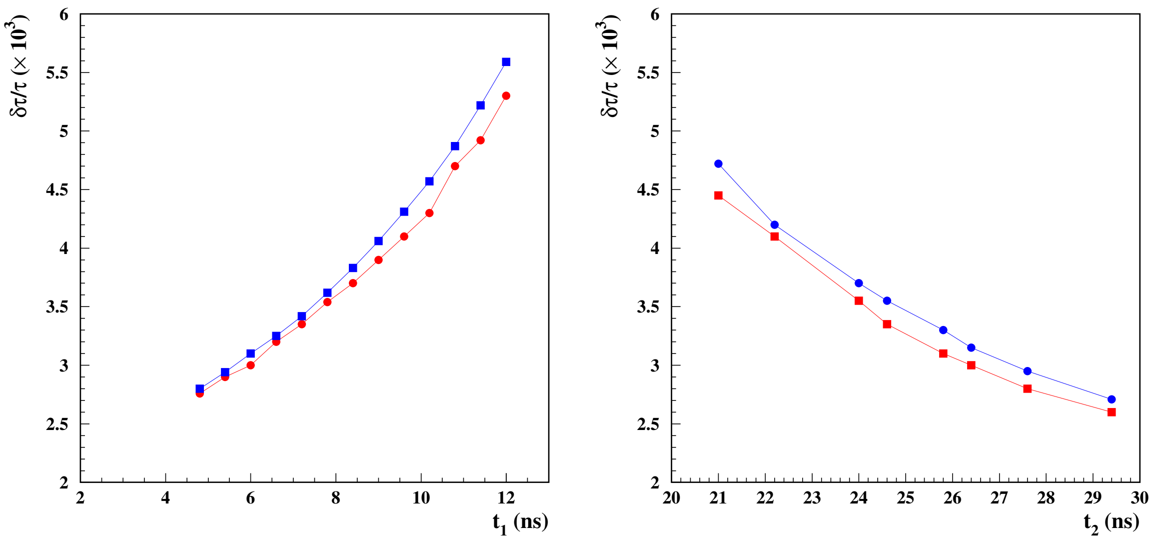

Figure 30: Statistical error as a function of fit limits. Left: the lower limit is moved, the upper is fixed. Right: the upper limit is moved, the lower is fixed. Blue squares are the results of the fit, red circles are the predictions as discussed in the text.

9 Analysis of systematic uncertainties

In order to extract the lifetime from a fit of the proper time distribution, we should have a pure and unbiased sample of decaying K_L 's. For the number of $K_L \rightarrow \pi^0\pi^0\pi^0$, $N_{\pi^0\pi^0\pi^0}$, we would like to have:

$$N_{\pi^0\pi^0\pi^0}(t^*) = N_{\pi^0\pi^0\pi^0}(t^* = 0)e^{-t^*/\tau_L} = N(\pi^0\pi^0\pi^0)(L_K = 0)e^{-L_K/\lambda} \tag{8}$$

where $\lambda = p\tau/M_K$ is the K_L mean decay length. At the end of the selection we have:

$$N(l) \;=\; N_{\pi^0\pi^0\pi^0}(L_K = 0) \cdot \int f(L'_K) \cdot e^{-L'_K/\lambda'} \cdot g(L_K - L'_K)dL'_K + N_{back} \tag{9}$$

where:

- N_{back} is the residual background at the end of the $\pi^0\pi^0\pi^0$ selection;
- $f(L'_K)$ is the efficiency function for signal;
- $g(L_K - L'_K)$ is the vertex resolution function;
- λ' is the effective mean path length taking into account also the K_L nuclear interactions in the drift chamber material.

These experimental effects bias the proper time distribution and must be properly taken into account. The accuracy reachable in their knowledge gives the systematic uncertainty in the measurement of the lifetime. In the following subsections each of these points is analysed in detail.

9.1 Systematic uncertainty due to the efficiency function

This analysis has been performed by maintaining the efficiency on the signal as high as possible in order to minimise its relative variations along the decay path. In fact, any selection cut produces an efficiency dependence along the fiducial volume that can modify the decay vertex distribution.

In the simplest case of an efficiency with a small linear dependence on L, $\epsilon(L) = a + bL$, we have that the number of K_L at L, $N(L)$, is given by:

$$\begin{aligned} N(L) &= N_0 e^{-L/\lambda} \cdot \epsilon(L) = N_0 e^{-L/\lambda} \cdot (a + bL) \\ &\simeq (N_0 \cdot a)(1 - L/\lambda)(1 + (b/a)L) \simeq (N_0 \cdot a) \cdot e^{-L/\lambda^*} \end{aligned} \tag{10}$$

with:

$$\lambda^* \sim \lambda(1 + (b/a)\lambda) \tag{11}$$

For example, for $\lambda \sim 340$ cm, if $(b/a) \sim 10^{-5}$/cm, we measure $\lambda^* = 1.003 \cdot \lambda$, i.e. a factor 0.3% higher than the true value.

Moreover, the statistical uncertainty of the b and a parameters introduces a systematic uncertainty in the knowledge of λ^*:

$$\frac{\delta\lambda^*}{\lambda^*} \sim \lambda \times \frac{b}{a} \times \left(\frac{\delta b}{b} \oplus \frac{\delta a}{a}\right) \tag{12}$$

In our case, the efficiency function is given by the convolution of three effect:

1. the tagging efficiency;
2. the preselection efficiency;
3. the selection efficiency.

In the following sections we will evaluate the corrections to be applied and the corresponding systematic uncertainties.

9.1.1 Tagging efficiency

The tagging efficiency has been parametrized in the FV as a function of L_K as a straight line with an intercept $a = (0.6804 \pm 0.0003)$ and a slope $b = (1.2 \pm 0.2) \cdot 10^{-5}$ (Fig. 6). From Eq. 11 we apply a correction on the lifetime value of $(b/a) \cdot \lambda = -0.6\%$.

The origin of the slope is due to a dependence of the trigger efficiency on the K_L decay position in the fiducial volume. The stability of this dependence has been checked by moving the only cut that can affect the trigger response, which is the the minimum energy threshold required for a pion cluster. In the standard selection we require to have at least one cluster on the calorimeter associated to a pion track with an energy $E \geq E_{thr}$, with $E_{thr} = 50$ MeV. We move this threshold from 40 MeV to 70 MeV at 10 MeV steps. The results are shown in Fig. 31.

The slopes change of $\delta b = 0.5 \cdot 10^{-5}$/cm when we move the energy threshold from $E_{thr} = 40$ MeV to $E_{thr} = 70$ MeV .

Therefore we assign a systematic uncertainty due to this spread, of $\delta\lambda/\lambda \sim (b/a) \cdot \lambda \cdot (\delta b/b) \sim 0.25\%$.

9.1.2 Preselection efficiency

The event preselection requires to have at least three neutral clusters with $E \geq 20$ MeV connected with the same vertex within $5{\cdot}\sigma$. The vertex reconstruction efficiency

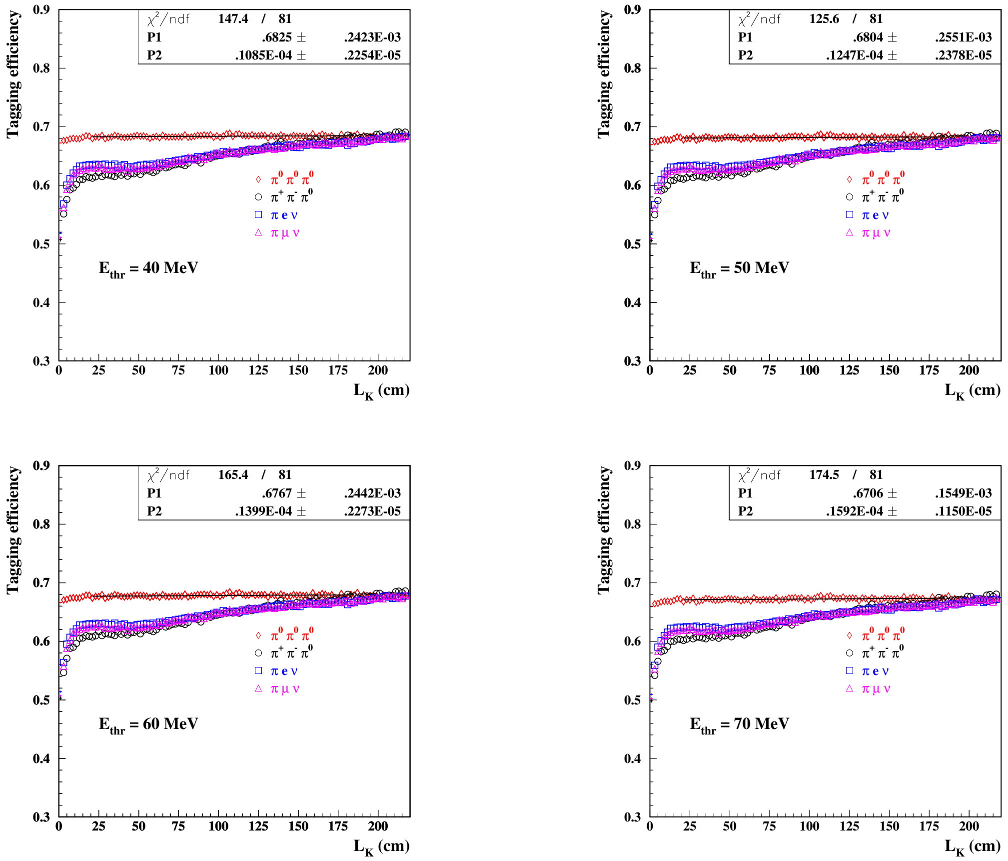

Figure 31: Tagging efficiency as a function of the K_L path length for the dominant K_L decay modes for E_{thr} = 40, 50, 60, 70 MeV.

has a linear dependence on L with an offset of $\sim$ 0.992 and a negative slope of $\sim -1.9 \cdot 10^{-5}$/cm (Fig. 19). Therefore, if $\lambda \sim$ 340 cm, λ^* comes out to be $\sim$ 0.65% lower. This effect has been taken into account by correcting bin by bin the decay path distribution with the vertex reconstruction efficiency values given by the Eq. 4. The statistical error of the efficiency values evaluated by Monte Carlo for $K_L \rightarrow \pi^0\pi^0\pi^0$ events has been added in quadrature to the statistical uncertainty of each bin of the proper time distribution.

The ratio $\epsilon(\pi^+\pi^-\pi^0\,, \text{data})/\epsilon(\pi^+\pi^-\pi^0\,, \text{MC})$ is flat in the fiducial volume (i.e. has a slope compatible with zero within its statistical error, see Fig. 20, right) and therefore does not move the central value of the fit. Nevertheless the statistical accuracy in the knowledge of this slope, $\sim 0.6 \cdot 10^{-5}$/cm gives a systematic uncertainty in the fit value of $\sim$ 0.2%.

In order to study the behaviour of the efficiency dependence with L_K as a function of the cluster energy threshold, E_{thr}, we move E_{thr} from 7 MeV to 35 MeV. The results are shown in Fig. 32. The slope changes from 0 to $\sim -2.3 \cdot 10^{-5}$/cm by moving E_{thr} from 10 MeV to 35 MeV. This is due to the fact that the hardening of the cut produces an event loss which does not distribute uniformely in the FV.

The energy cut changes the relative weight of events with 3,4,5,6,7,$\geq$8 photons as it is shown in Fig. 35: the signal losses come from events with three photons that, increasing the threshold, loose a photon and are, therefore, rejected.

The variation of this cut produces also a variation of the background contamination. This is clear from Fig. 33 (left) where we show the energy spectrum for signal and background for $E_{thr} = 10$ MeV. The background distribution is peaked at low energy and, therefore, is very sensitive to the threshold (Fig. 33, right). In fact, if we plot the relative variation of the event losses and background contamination in FV as a function of E_{thr} by taking as reference the values at $E_{thr} = 20$ MeV, we have that the background contamination from 10 MeV to 35 MeV is reduced by $\sim 160\%$ while the signal losses are of the order of few per mil (Fig. 34).

For each E_{thr} we fit the K_L proper time distribution after background subtraction and efficiency correction. The results are shown in Fig. 36 both for data and Monte Carlo by taking as reference the values at 20 MeV. We see that for data the fit result is stable down to 15 MeV. Below 15 MeV there is a decreasing of $\sim 0.5\%$ due to the fact the amount of background evaluated by Monte Carlo is not more reliable. We take as systematic uncertainty in the fit result the variation of the mean values among 15 MeV and 35 MeV, $\sim 0.2\%$.

Finally, the systematic uncertainty on the preselection efficiency evaluation is $0.2\% \oplus 0.2\% = 0.3\%$.

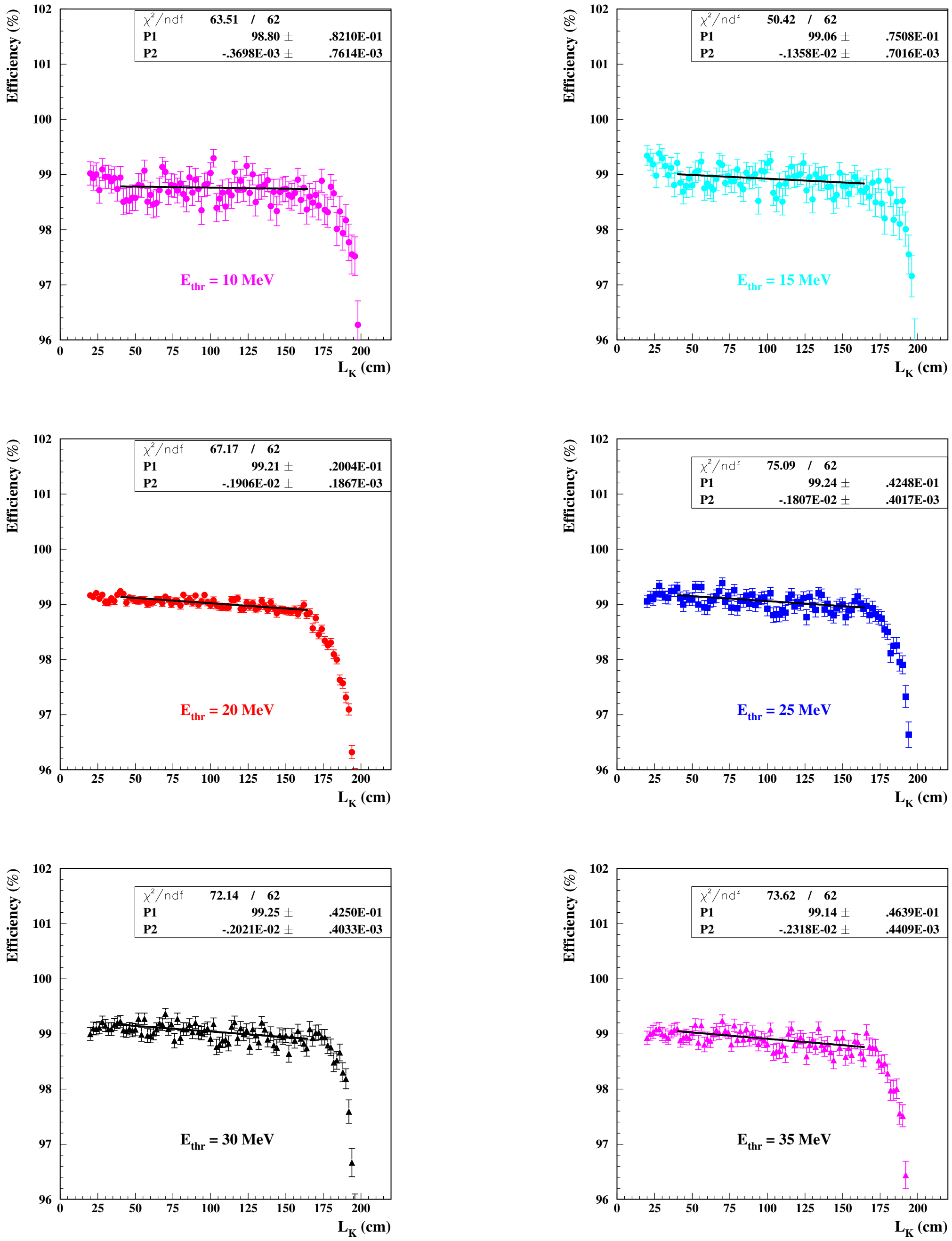

Figure 32: Vertex reconstruction efficiency for $K_L \rightarrow \pi^0\pi^0\pi^0$ Monte Carlo sample as a function of the decay path length for different cluster energy thresholds.

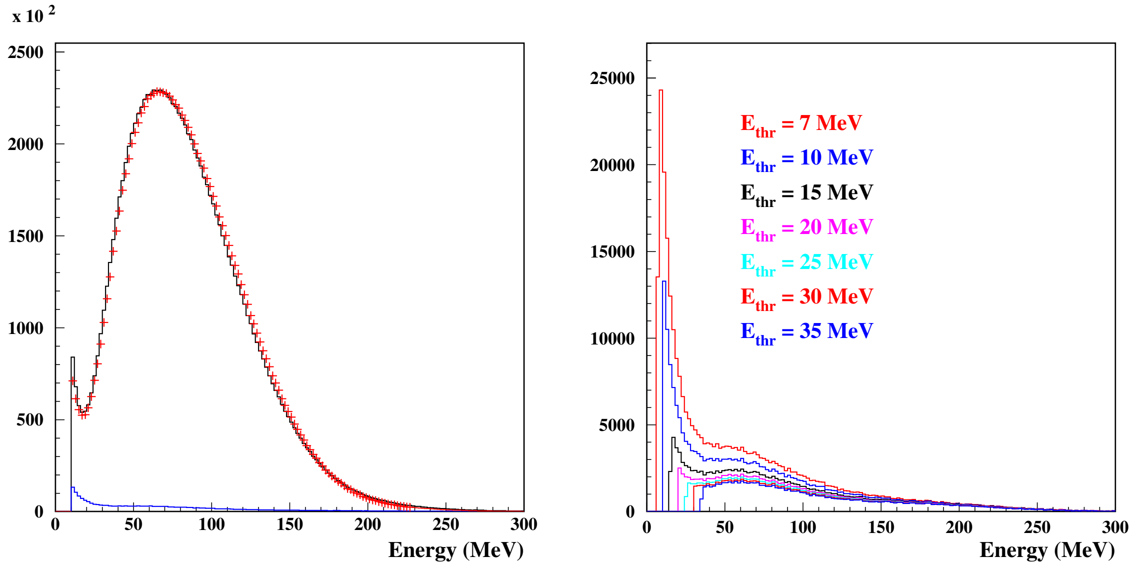

Figure 33: Left: energy distribution at the end of the selection. Red crosses are data, black histogram is Monte Carlo signal+background, blue histogram is Monte Carlo background. Right: zoom of the background energy distribution for several energy thresholds.

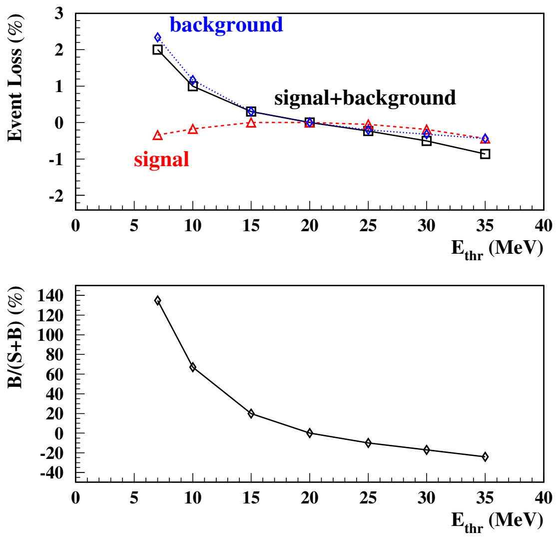

Figure 34: Up: Event loss in FV as a function of E_{thr} from Monte Carlo for signal (red triangles), background (blue rhombs) and signal+background (black squares). Down: background contamination in FV as a function of E_{thr}. All the values are relative to the E_{thr}=20 MeV cut.

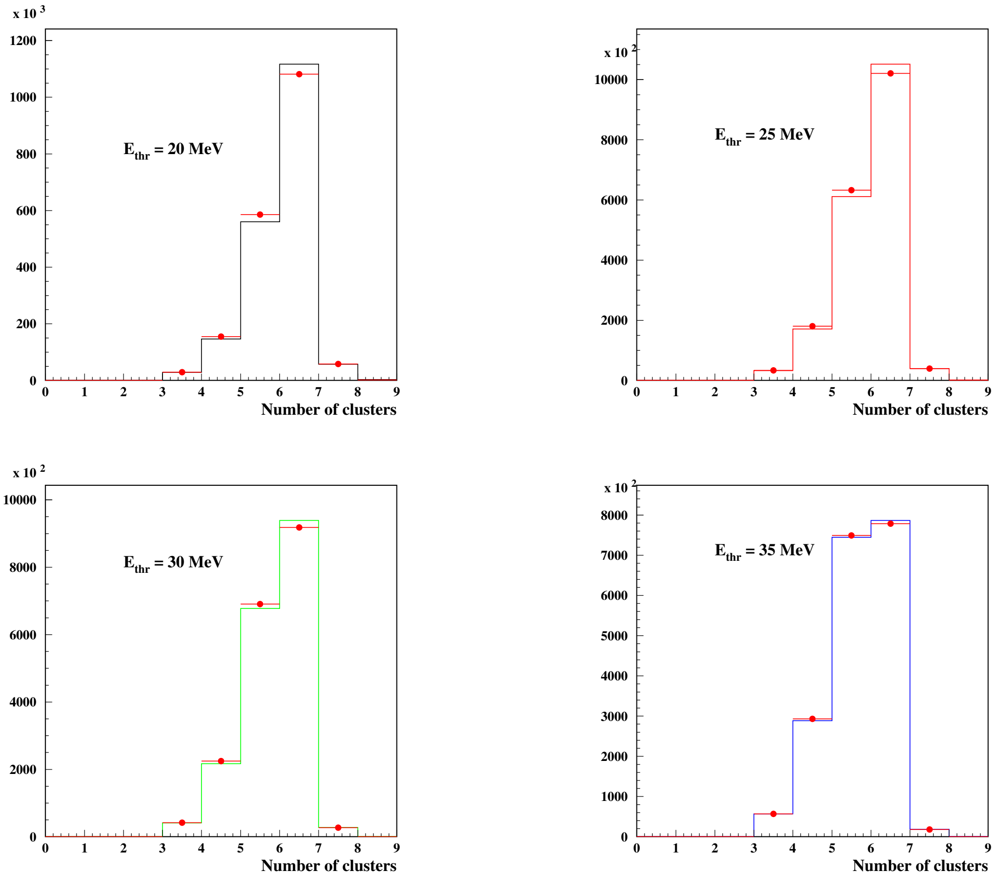

Figure 35: Cluster multeplicities as a function of E_{thr}. Red dots are data, solid histograms are Monte Carlo.

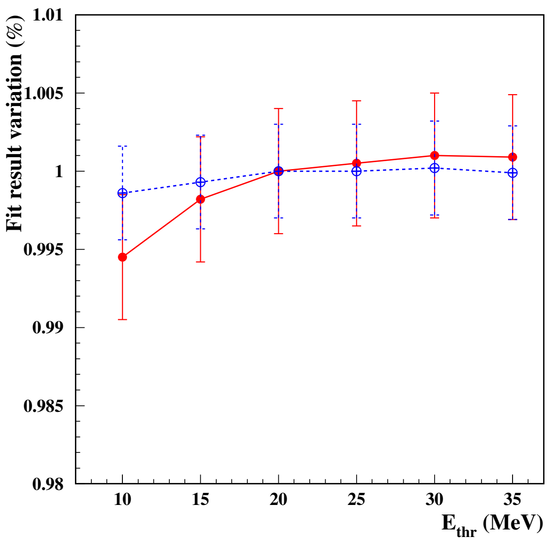

Figure 36: Fit result variation as a function of E_{thr}. Blue dots are Monte Carlo, Red dots are data.

9.1.3 Selection efficiency

The selection cuts are applied only on events with $N = 3$ photons connected to the same vertex. They are the ~ 1 % of the total number of events. These cuts produce an inefficiency of $1\% \times (1-\epsilon) = 1\% \times (1-55\%) \sim 0.5\%$ on the total event sample.

The efficiency variation with L_K (Fig. 25) is taken into account by weighting the events with $N = 3$ photons at a given L_K with the inverse of the efficiency evaluated in the same point. Since the efficiency is evaluated using Monte Carlo we assign as systematic uncertainty the accuracy in the knowledge of the signal in the Monte Carlo. This accuracy has been evaluated by comparing the data-Monte Carlo L_K distributions for the $N = 5$ and $N = 6$ samples that are background free. The results are shown in Fig. 37. The rms of the data-Monte Carlo ratios distributions in FV is $\sim 1\%$. The systematic uncertainty due to event selection is, therefore, $0.5\% \times 1\% = 5 \cdot 10^{-5}$, i.e. fully negligible.

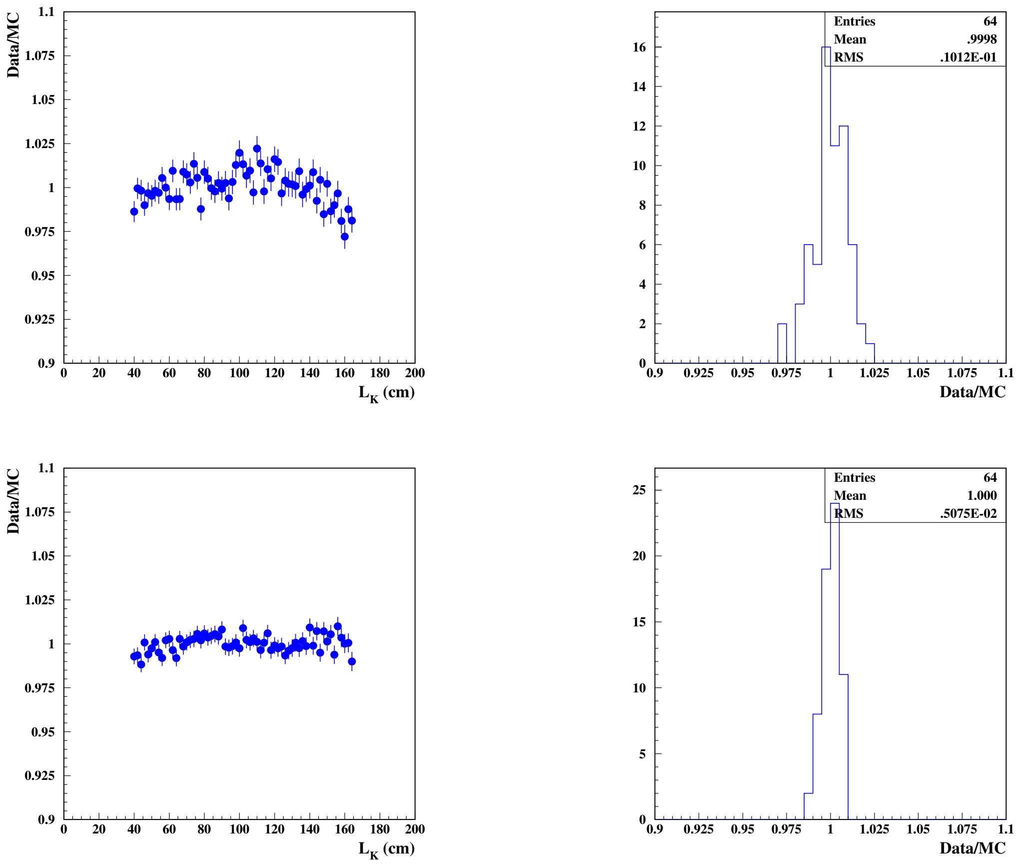

Figure 37: Data/Monte Carlo ratio for the decay path distributions for the $N = 5$ (up) and $N = 6$ (down) event samples.

9.2 Systematic uncertainty due to the vertex resolution

The K_L vertex resolution has been measured with the $K_L \rightarrow \pi^+\pi^-\pi^0$ data sample. The resolution depends on the cluster energies and on the K_L decay path.

In the case of a fit with a simple gaussian (Fig. 15) the vertex resolution as a function of L_K goes as:

$$\sigma(L_K) = (1.65 + 0.6 \cdot 10^{-2}/\mathrm{cm} \times L_K + 0.45 \cdot 10^{-4}/\mathrm{cm}^2 \cdot L_K^2)\ \mathrm{cm} \tag{13}$$

while in the case of a double gaussian fit the behaviour is shown in Fig. 16, left.

The effect of the resolution on the fit value has been studied by smearing the values extracted from an exponential function with the measured σ's, parametrised as a function of l_K (see Fig. 15 and Fig. 16), both in the case of a simple gaussian fit and in the case of a double gaussian fit. In this second case, the smearing is performed by taking into account the relative weights of the two gaussians at a given L_K (Fig. 16, right). The measured resolution has been multiplied artificially by a scale factor 1.5, 2, 2.5 to investigate the behaviour of the fit result (Fig. 38, right).

The relative variation of the fit value for $1{\cdot}\sigma$ in both cases (simple and double gaussian fit) is below 0.1%. The σ are known, in the worse case of the double gaussian fit, at 1-2 % level (see Fig. 14, right). We assume as systematic uncertainty on the fit result due to the vertex resolution the variation of the fit due to a variation of the σ of 10 % around their mean values. This variation of the fit is $\sim 0.1\%$.

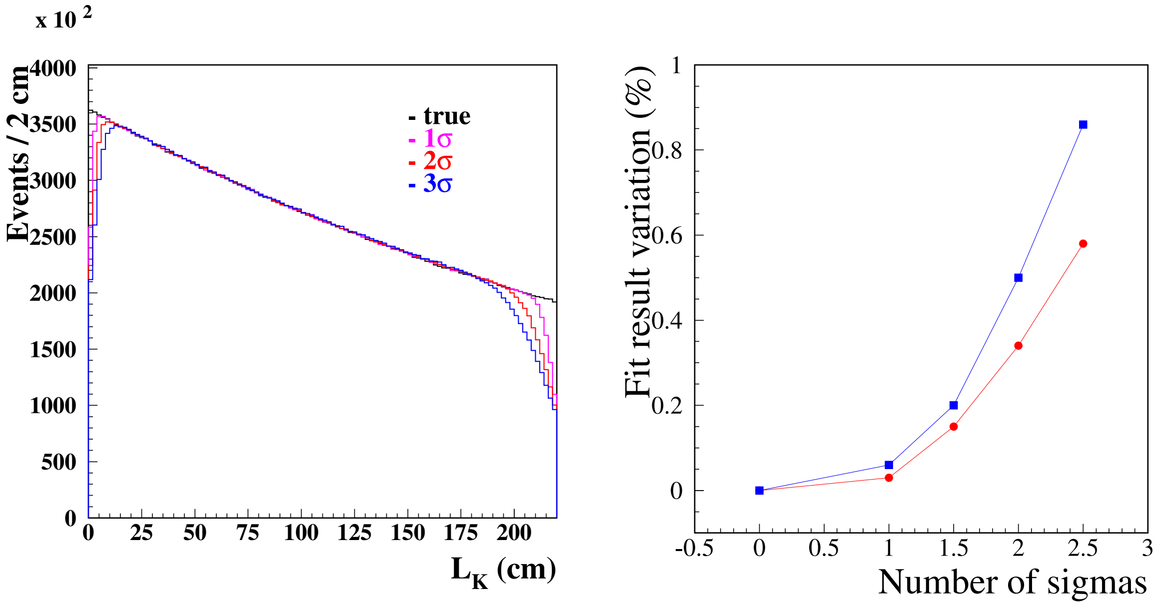

Figure 38: Effect of the vertex resolution on the decay length distribution (left) and relative variation of the fit result with the resolution (right) in the case of a single gaussian (red dots) and double gaussian (blue squares).

9.3 Systematic uncertainty due to the absolute time scale calibration

In Section 5.3 we show that the difference between the K_L vertex position reconstructed by the calorimeter and the one reconstructed by the chamber for $K_L \rightarrow \pi^+\pi^-\pi^0$ events has on average an offset $a = 2$ mm and a slope $b = (-0.7 \pm 0.7) \cdot 10^{-4}$ (Fig. 17). Since the slope is compatible with zero, this correction does not move the fit value but, anyhow, introduces a systematic uncertainty due to the statistical uncertainty on the slope. In fact we have that:

$$L_K(\text{measured}) = a + L_K(\text{true}) \cdot (1 + (b \pm \delta b))$$

and therefore:

$$e^{(-L_K(\text{measured})/\lambda)} = Ae^{(-L_K(\text{true})/\lambda')}$$

where:

$$\lambda' \sim \lambda \cdot (1 \pm \delta b)$$

Therefore we assign a systematic uncertainty on the lifetime due to the knowledge of the time scale of 0.7×10^{-4}.

9.4 Systematic uncertainty due to the background subtraction

The background contamination $k = B/(S+B)$ after the signal selection is ~ 1.3 %, mainly concentrated in the $N = 3$ and $N = 4$ event samples (see Section 6, Table 2).

This residual background must be kept under control since the fit result is very sensitive to it. In Fig. 39 we show the relative variation of the fit result (red circles) as a function of k and we see that the dependence is linear with a slope of ~ 1.1, i.e. a $k \sim 1\%$ produces an increase of the lifetime value of ~ 1.1 %. Moreover, the proper time distribution deviates from an exponential function and this reflects in an increase of the normalized χ^2 (Fig. 39, blue triangles).

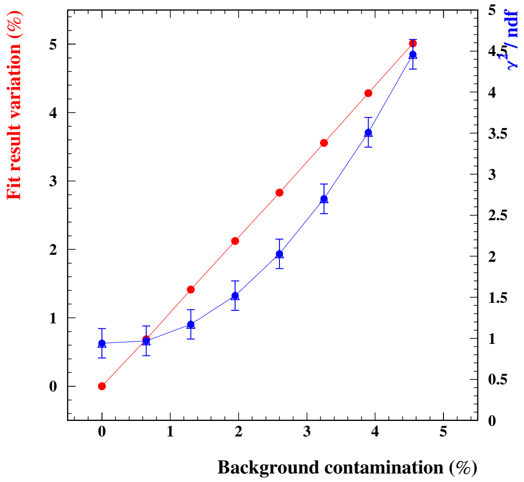

Figure 39: Relative variation of the lifetime value (red circles) and normalized χ^2 (blue triangles) as a function of the background contamination.

The residual background is subtracted bin by bin from the proper time distribution using Monte Carlo simulation (see Fig. 26 and Fig. 23). A systematic error arises from the uncertainty in the background knowledge. In Fig. 40 we show the relative variation of the fit value as a function of the accuracy in the background knowledge.

In order to study this accuracy, we subtract from the decay path distributions of the $N = 3$ and $N = 4$ samples the contribution of the $K_L \to \pi^0\pi^0\pi^0$ signal. The results are shown in Fig. 41 for the $N = 3$ sample, in Fig. 42 for the $N = 4$ sample and in Fig. 43 for the $N = 3 + 4$ samples. On the right side of these plots we show the distributions of the ratios obtained dividing bin by bin the data and Monte Carlo distributions. From Fig. 43, right we see that the distribution of the ratios is peaked at 1.02 with an rms of 10%. Although data and Monte Carlo agree on the background level to within $\sim 2\%$, we have conservately taken the uncertainty in the backgorund scale to be $\sim 10\%$. From Fig.40 a variation of the background scale of 10% produces a systematic uncertainty in the lifetime of $\sim 0.2\%$.

Moreover this ratio has a slope as a function of L_K of $(-0.61 \pm 0.08) \cdot 10^{-3}$/cm.

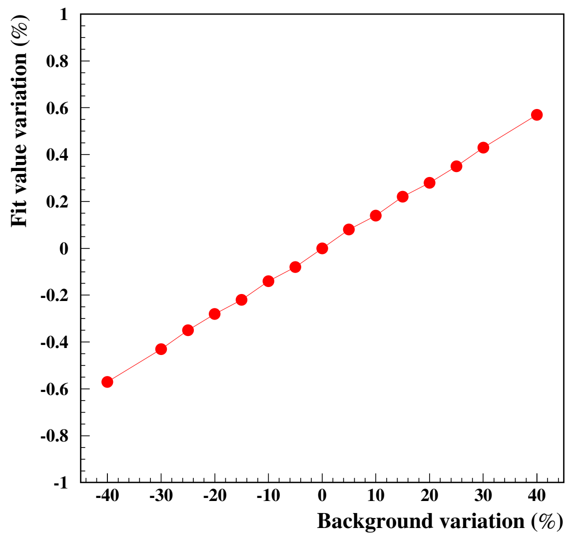

Figure 40: Relative variation of the lifetime value as a function of the accuracy in the knowledge of background.

If we correct for this slope the background distribution obtained from Monte Carlo before subtract it to the proper time distribution obtained with data, the lifetime value increases of 0.15% with a systematic uncertainty due to the statistical error on this slope of 0.06%.

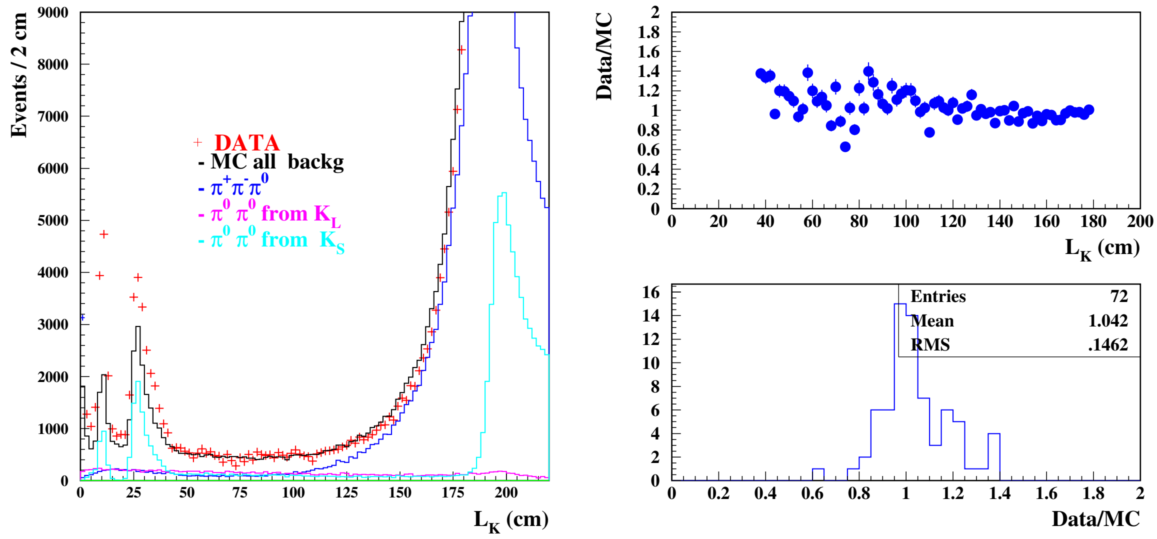

Figure 41: Left: decay length distribution for background with $N = 3$ photons. Red crosses are data, solid histogram are Monte Carlo. The contributions from different decay channels are shown as coloured histograms. Right: data/Monte Carlo ratios in the FV.

In order to check for possible systematic effects due to different contamination of the background in different zones of the fiducial volume (in particular the $K_L \to \pi^+\pi^-\pi^0$

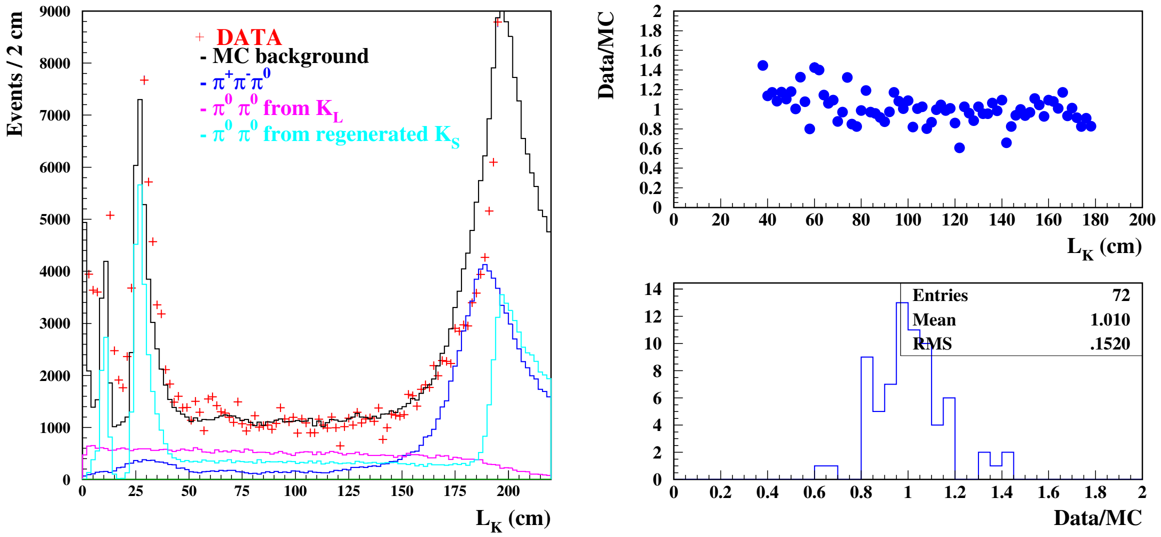

Figure 42: Left: decay length distribution for background with $N = 4$ photons. Red crosses are data, solid histogram are Monte Carlo. The contributions from different decay channels are shown as coloured histograms. Right: data/Monte Carlo ratios in the fiducial volume.

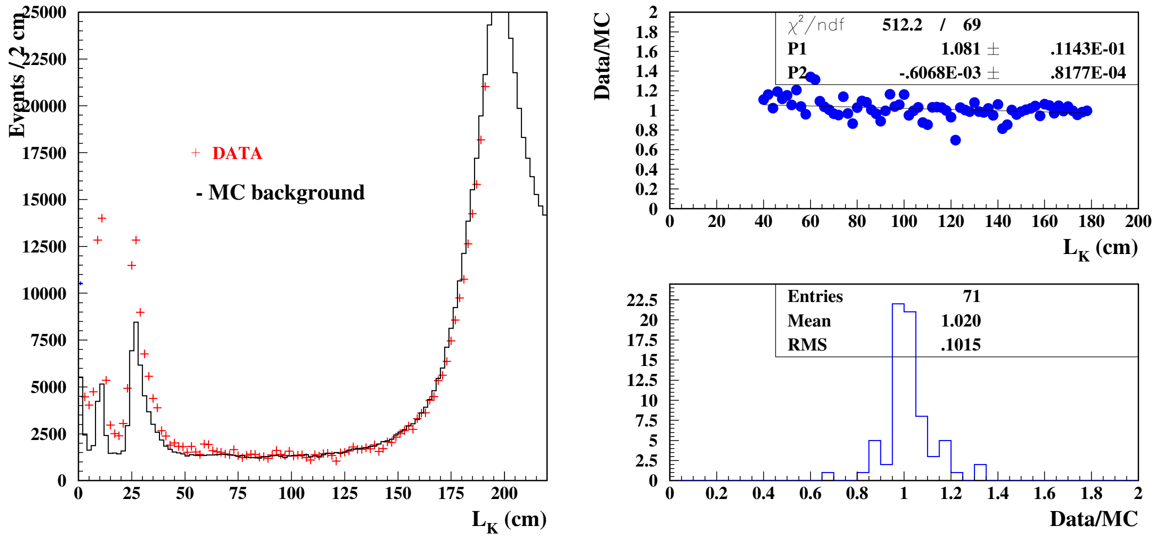

Figure 43: Left: decay length distribution for background with $N = 3 + 4$ photons. Red crosses are data, solid histogram are Monte Carlo. Right: data/Monte Carlo ratios in the fiducial volume.

background which mainly affects the external boundary of the drift chamber at low θ angles) we divide the FV in two parts in θ and perform the fit. The FV is divided in such a way that the two parts contain the same number of events. Since $dN/d(\cos\theta) \propto \sin^2(\theta)d(\cos(\theta))$ and the $\theta(min) = 21°$ due to the presence of QCALs, this condition is satisfied by the two regions:

1. $21° < \theta < 70°$ and $110° < \theta < 159°$;
2. $70° < \theta < 140°$.

The results are shown in Fig. 44: they are compatible within the errors.

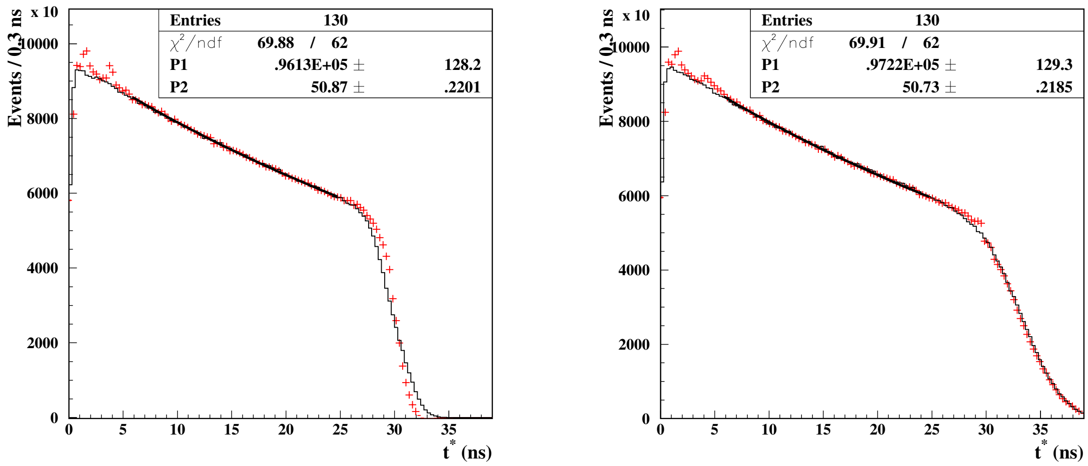

Figure 44: K_L proper time distributions for the two regions of the FV as explained in the text.

9.5 Systematic uncertainty due to the K_L nuclear interactions

The rates for the dominant K_L nuclear interaction processes (regeneration, Λ and Σ production) are determined using data (Ref. [4]) and the simulation is corrected accordingly. In particular the contribution of the regeneration in the drift chamber material has been found to be a factor 3 less abundant in data than in Monte Carlo and the one from $\Lambda\pi^0$ production a factor 10. In data the sum of all the nuclear interactions amounts to $\sim 0.33\%$ where we apply a conservative error of 50%, $(0.33\pm0.16)\%$. Therefore, from Eq.7, we have that the K_L lifetime must be corrected by $+0.33\%$ with a systematic uncertainty of 0.16%.

9.6 Variation of the fit result with the fit limits

In order to study the stability of the fit value with the fit limits we move the limits one at the time by maintaining the other fixed at the nominal value (6 ns or 24.8 ns). The results are shown in Fig. 45 (up). In Fig. 45 (down) we also show the behavior of the normalized χ^2. We notice that:

- below 6 ns the result of the fit tends towards lower values as a consequence of the bad simulation of the amount of the background contribution coming from $K_S \to \pi^0\pi^0$ events from $K_L \to K_S$ regeneration in the inner wall of the drift chamber. This background affects mainly the $N = 3$ and $N = 4$. (see Fig. 23 for $N = 4$ and Fig. 26 for $N = 3$).

- the fit is stable up to $t_2 = 27.5$ ns well above the chosen upper limit of $t_2 = 24.8$ns. Anyway, we prefer do not extend this limit in order do not increase systematic uncertainties due to the poor knowledge of the vertex reconstruction efficiency and the background contamination in the external boundary of the FV.

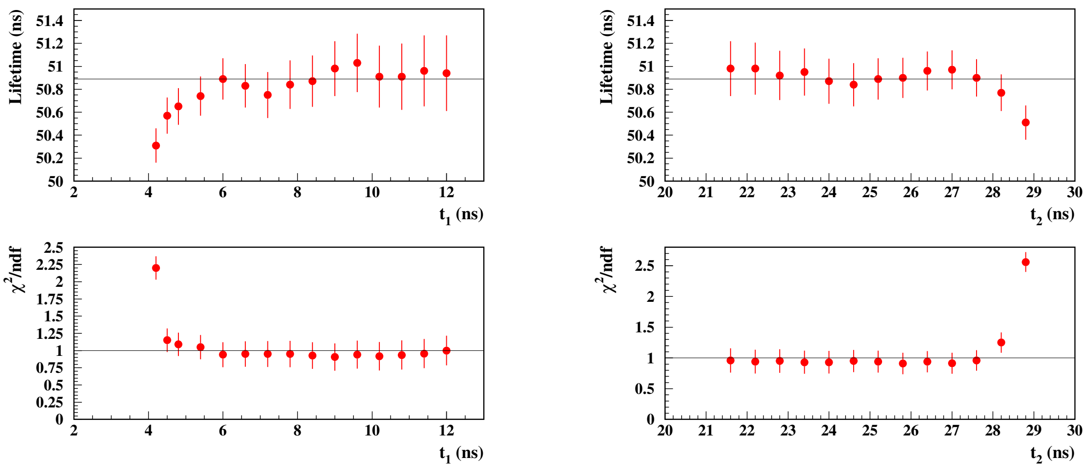

Figure 45: Fit result and normalized χ^2 as a function of the fit limits.

9.7 Summary of systematic uncertainties and lifetime result

In Table 4 we show the corrections to be applied to the lifetime fit result and the corresponding systematic uncertainties. The corrections due to the preselection efficiency, the selection efficiency and the background subtraction have been applied on a bin by bin basis.

A residual correction of 0.2% due to background subtraction has been added due to the fact that the background from the K_S regeneration in the drift chamber material is a factor three higher in the Monte Carlo than in data (see Section 9.5). Therefore, from Table 2, the 0.29% contribution of $K_L \to K_S \to \pi^0\pi^0$ reaction must be reduced to 0.1% and the global amount of background contamination from 1.3 % to 1.1%. This has as direct effect to increase the fit value of +0.2%.

The uncertainty in the momentum scale calibration of the drift chamber enters directly in the proper time evaluation $t^* = L_K/(\beta\gamma c)$ and produces a systematic error of $\pm 0.1\%$ [3].

source	correction	systematic uncertainty
tagging efficiency	- 0.6%	$\pm 0.25\%$
preselection efficiency	bin by bin	$\pm 0.3\%$
selection efficiency	bin by bin	$\pm 5 \cdot 10^{-5}$
vertex resolution	-	$\pm 0.1\%$
momentum scale	-	$\pm 0.1\%$
time scale	-	$\pm 0.07\%$
background scale	bin by bin + 0.2%	$\pm 0.2\%$
background shape	+ 0.15%	$\pm 0.06\%$
nuclear interactions	+ 0.33%	$\pm 0.16\%$
total	+0.1%	0.49%

Table 4: Summary of corrections and systematic uncertainties.

We can notice that the corrections sum to ~ 0 and, therefore, the central value of the fit is not moved. We see also that the systematic error is dominated by the uncertainty of the dependence of tagging efficiency and preselection efficiency with L_K and by the background subtraction.

Putting all together we have that the K_L lifetime value is:

$$\tau_{K_L} = (50.92 \pm 0.17_{\text{stat}} \pm 0.25_{\text{syst}})\text{ns} = (50.92 \pm 0.30)\text{ns}$$

This result is compatible at 1.3 σ level with the other direct measurement $\tau_{K_L} = (51.54 \pm 0.44)$ ns (Ref. [1]) and is compatible only at ~ 1.7 σ level with the PDG 2004 fit result, $\tau_{K_L} = (51.8 \pm 0.4)$ ns.

10 Effect of the K_L lifetime on CKM parameter $|V_{us}|$

The determinations of $|V_{us}|$ and $|V_{ud}|$ provide the most precise test of CKM unitarity, the contribution of the error of $|V_{ud}|$ being at the level of $\sim 10^{-5}$. $|V_{us}|$ is proportional to the square root of the semileptonic BR of K mesons. For K_L^{e3} decays we can write (Ref. [7]):

$$|V_{us}| \times f_+^{K^0\pi}(0) = \left[\frac{128\pi^3 BR(K_L \to \pi e\nu)}{\tau_L G_\mu^2 M^5 S_{ew} I_K^e(\lambda_+, \lambda'_+)}\right]^{1/2} \times \frac{1}{1+\delta_{\rm em}^{Ke}} \tag{14}$$

where $f_+^{K^0}(0)$ is the normalisation of the kaon form factors at zero momentum transfer and $I_i(\lambda_+, \lambda'_+)$ is the integral of the phase space density, factoring out $f_+^{K^0\pi}$ and without radiative corrections. Radiative corrections at large scale of form factor and phase space density are contained in the term $\delta_{em}^{Ke} = (0.55 \pm 0.10)\%$ (Refs. [8, 9]). The short-distance electroweak corrections are included in the parameter S_{ew}. λ_+ and λ'_+ are the slope and curvature of the vector form factor $f_+^{K^0\pi}(0)$. From eq. 14 we see that the lifetime value enters directly in the determination of the product $|V_{us}| \times f_+^{K^0\pi}(0)$ both as far as regard the error and the central value. The three most recent results [10],[12],[4] are:

$$\begin{array}{lll} BR(K_L \to \pi e\nu) & = (40.67 \pm 0.11)\% & \text{KTeV} \\ BR(K_L \to \pi e\nu) & = (40.10 \pm 0.45)\% & \text{NA48} \\ BR(K_L \to \pi e\nu) & = (40.07 \pm 0.15)\% & \text{KLOE} \end{array}$$

where the error is the sum in quadrature of the statistical and systematic uncertainties. Fig. 46 (left) shows the product $|V_{us}| \times f_+^{K^0\pi}(0)$ extracted from the three recent measurements of $BR(K_L \to \pi e\nu)$ using the most precise published measurement of the K_L lifetime, $\tau = (51.54 \pm 0.44)$ ns (Ref. [1]). In the extraction of V_{us} we use the values of λ_+ and λ'_+ obtained by KTeV experiment from a quadratic fit (Ref. [13]). In the same plot we show also the value of $|V_{us}| \times f_+^{K^0\pi}(0)$ obtained from the KLOE preliminary measurement of $BR(K_S \to \pi e\nu) = (7.09 \pm 0.07_{stat} \pm 0.08_{syst}) \cdot 10^{-4}$ (Ref. [14]) and the $\pm 1\sigma$ band from the $|V_{ud}|$ and unitarity where we assume $f_+^{K^0\pi}(0) = 0.961 \pm 0.008$ (Ref. [15]). Fig. 46 (right) shows the same product extracted using the KLOE K_L lifetime value, $\tau_L = (50.92 \pm 0.17 \pm 0.25)$ ns. The K_L data are much more in agreement with K_S and unitarity.

11 Conclusions

We have done a direct measurement of the K_L lifetime with the $K_L \to \pi^0\pi^0\pi^0$ decays tagged by $K_S \to \pi^+\pi^-$ events. With a data sample of ~ 400 pb^{-1} of integrated luminosity we find $\tau = (50.92 \pm 0.17_{\rm stat} \pm 0.25_{\rm syst})$ ns. This result is compatible with the most precise published direct measurement $\tau = (51.54 \pm 0.44)$ ns [1] at 1.2σ level

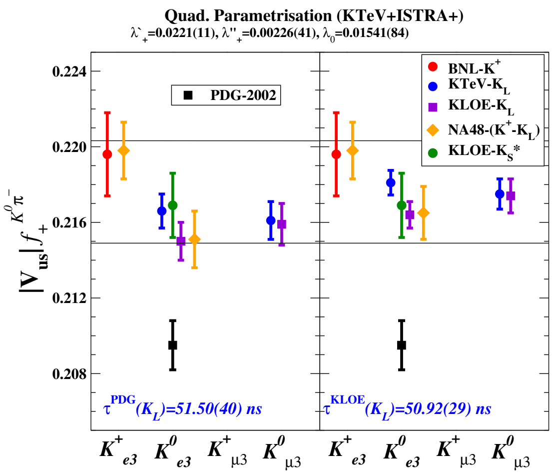

Figure 46: The product $|V_{us}|\times f_+^{K^0\pi}(0)$ from the three recent measurements of the $BR(K_L \to \pi e\nu\,)$ for two most precise direct measurements of the K_L lifetime. The value obtained from $BR(K_S \to \pi e\nu\,)$ and the $\pm 1\sigma$ band obtained from $|V_{ud}|$ and unitarity is also shown.

and compatible within 2σ with the result obtained with the PDG 2004 fit. The value of the lifetime has been used to extract the product $|V_{us}| \times f_+^{K^0\pi}(0)$ from the three recent measurements of the $BR(K_L \to \pi e\nu\,)$ ([10],[12],[4]): the three values obtained from K_L semileptonic decays are much more compatible with the one obtained from $K_S \to \pi e\nu$ branching fraction [14] and from $|V_{ud}|$ and unitarity.

12 Acknowledgements

This analysis could not be done without the help of many people of the Neutral Kaon KLOE Working Group and I want to thank all of them. In particular I want to warmly aknowledge Prof. P. Franzini for helping me in performing the lifetime fit and estimate its statistical error, Dr. G. Capon for giving me the hint that background could be reduced by an optimal choice of the fiducial volume, Dr. M. Moulson and Dr. T. Spadaro for providing me their *kcp* libraries, Dr. C. Gatti and Dr. C. Bloise for evaluation of the effect of the K_L nuclear interactions in the lifetime measurement, Dr. M. Palutan for interesting comments on the bunch crossing identification and all the others for very interesting discussions and suggestions that helped me to finalise this job. I want also to thank Dr. A. Di Domenico, my internal referee, for his patience in correcting this note and the relative paper.

References

[1] K.G. Vosburgh *et al.*, Phys. Rev. Lett. **26** (1971), 866 and Phys. Rev. D6 (1972), 1834.

[2] P. Franzini, *Predicting the statistical accuracy of an experiment*, The Second DAΦNE Physics Handbook, Vol. II, p.823, ed. L. Maiani, G. Pancheri, N. Paver (1995). See also *Statistics, The method of maximum likelihood*, in Review of Particle Physics, Phys. Lett. B 592 (2004).

[3] A. Ambrosino et al., Nucl. Instr. Meth. **A534** (2004), 403-433.

[4] M. Antonelli, P.Beltrame, M.Dreucci, M. Moulson, M. Palutan, A. Sibidanov, *Measurements of the Absolute Branching Ratios for dominant K_L decays, the K_L lifetime and V_{us} with the KLOE detector*, KLOE memo n.302 (2005).

[5] The KLOE Collaboration, M. Adinolfi et al., *The Trigger System of the KLOE experiment*, Nucl. Instr. and Meth. A492 (2002) 134.

[6] S. Di Falco, G. Lanfranchi, E. Santovetti *Measurement of the ratio $\Gamma(K_L \to \gamma\gamma)/\Gamma(K_L \to \pi^0\pi^0\pi^0)$ with the KLOE detector*, Kloe Note n. 182 and Phys. Lett. B 566 (2003), 61.

[7] M. Battaglia *et al.*, arXiv: hep-ph/0304132.

[8] V. Cirigliano *et al.*, *Eur. Phys. J. C***23**,121 (2002).

[9] V. Cirigliano *et al.*, *Eur. Phys. J. C***35**,53 (2004).

[10] T. Alexopoulos et al. (KTeV Collaboration), Phys. Rev. **D70** (2004), 092006 .

[11] S. Eidelman et al., Phys. Lett. B592 (2004) 1

[12] A. Lai et al. (NA48 Collaboration), *Measurement of the branching ratio of the $K_L \to \pi e \nu$ decay and extraction of the CKM parameter $|V_{us}|$.*, Phys. Lett. B602 (2004), 41.

[13] T. Alexopoulos *et al.* [KTeV Collaboration], Phys. Rev. D70 092007, 2004.

[14] T. Spadaro on behalf of the KLOE Collaboration, talk at La Thuile 2004.

[15] H. Leutwyler, M. Roos, *Z. Phys.* C **25**, 91 (1984).

A Appendix

In the following tables we report bin by bin all the numbers necessary to compute the lifetime histogram and perform the fit. In particular:
column # 1: bin number;
column # 2: upper limit of the bin (1 bin = 0.3 ns);
column # 3: Number of data events (signal + background);
column # 4: Number of background events from Monte Carlo;
column # 5: Vertex reconstruction efficiency;
column # 6: Number of signal events after background subtraction and efficiency corrections;
column # 7: Value of the function $f(t) = p_1 \cdot e^{-t/p_2}$ in the center of the bin with $p_1 = (179692 \pm 180)$ events and $p_2 = (50.867 \pm 0.165)$ ns.
column # 8: Contribution to the χ^2 of each bin.

Bin #	t^* (ns)	$N \pm \delta N$ (Events/0.3ns)	$B \pm \delta B$ (Events/0.3ns)	$\epsilon \pm \delta\epsilon$ (%)	$S \pm \delta S$ (Events/0.3ns)	f (Events/0.3ns)	$\chi^2(i)$
1	.3	149930±387	4103± 64	69.16 ± .32	135561±393	179155.1	2311.987
2	.6	175498±419	1813± 43	90.27 ± .16	161501±421	178101.7	552.905
3	.9	175834±419	1130± 34	98.17 ± .08	177943±434	177054.5	4.185
4	1.2	176047±420	1384± 37	99.09 ± .06	176248±428	176013.5	.301
5	1.5	183122±428	3156± 56	98.97 ± .06	181792±440	174978.5	240.053
6	1.8	183763±429	4010± 63	99.08 ± .06	181354±441	173949.7	282.252
7	2.1	175180±419	1765± 42	99.16 ± .05	174859±427	172926.8	20.465
8	2.4	172039±415	934± 31	99.19 ± .05	172494±422	171910.0	.917
9	2.7	170956±413	903± 30	99.07 ± .06	171639±421	170899.2	3.077
10	3.0	169227±411	964± 31	99.16 ± .05	169670±419	169894.4	.287
11	3.3	168588±411	1049± 32	99.13 ± .06	168988±418	168895.4	.049
12	3.6	170170±413	2369± 49	99.20 ± .05	169111±421	167902.3	8.228
13	3.9	175508±419	5179± 72	99.10 ± .06	171793±432	166915.1	127.360
14	4.2	175401±419	6131± 78	99.17 ± .05	170586±433	165933.6	115.576
15	4.5	170550±413	5239± 72	99.04 ± .06	166832±427	164957.9	19.279
16	4.8	167670±409	3673± 61	99.03 ± .06	165545±421	163988.0	13.661
17	5.1	165175±406	2849± 53	99.11 ± .06	163746±417	163023.8	3.006
18	5.4	164341±405	2326± 48	99.06 ± .06	163519±415	162065.2	12.263
19	5.7	162304±403	2009± 45	99.17 ± .06	161601±411	161112.3	1.413
20	6.0	160312±400	1673± 41	99.24 ± .05	159831±408	160165.0	.671
21	6.3	159058±399	1429± 38	99.19 ± .06	158897±406	159223.2	.644
22	6.6	157792±397	1201± 35	99.03 ± .06	158107±406	158287.0	.197
23	6.9	156630±396	1175± 34	99.12 ± .06	156810±403	157356.3	1.830
24	7.2	156599±396	1111± 33	99.10 ± .06	156888±404	156431.0	1.280
25	7.5	155231±394	1032± 32	99.07 ± .06	155623±402	155511.2	.078

Table 5: .

Bin #	t_2 (ns)	$N \pm \delta N$ (Events/0.3ns)	$B \pm \delta B$ (Events/0.3ns)	$\epsilon \pm \delta\epsilon$ (%)	$S \pm \delta S$ (Events/0.3ns)	f (Events/0.3ns)	$\chi^2(i)$
26	7.8	154689 ± 393	1051 ± 32	99.05 ±.06	155092 ± 401	154596.8	1.520
27	8.1	153128 ± 391	1052 ± 32	99.08 ±.06	153464 ± 399	153687.8	.313
28	8.4	152668 ± 391	922 ± 30	99.08 ±.06	153144 ± 398	152784.2	.816
29	8.7	151899 ± 390	955 ± 31	99.01 ±.06	152446 ± 398	151885.8	1.982
30	9.0	150640 ± 388	1053 ± 32	99.03 ±.06	151037 ± 396	150992.7	.013
31	9.3	149972 ± 387	978 ± 31	99.05 ±.06	150415 ± 395	150104.9	.615
32	9.6	148331 ± 385	1088 ± 33	99.09 ±.06	148579 ± 393	149222.3	2.680
33	9.9	148063 ± 385	1079 ± 33	99.09 ±.06	148320 ± 392	148344.9	.004
34	10.2	146899 ± 383	1068 ± 33	99.02 ±.06	147258 ± 391	147472.6	.301
35	10.5	146598 ± 383	1090 ± 33	99.14 ±.06	146754 ± 390	146605.5	.144
36	10.8	145376 ± 381	1053 ± 32	99.09 ±.06	145637 ± 389	145743.5	.075
37	11.1	144849 ± 381	1027 ± 32	99.00 ±.06	145254 ± 389	144886.5	.892
38	11.4	143673 ± 379	967 ± 31	99.06 ±.06	144048 ± 387	144034.6	.001
39	11.7	142568 ± 378	957 ± 31	99.06 ±.06	142941 ± 385	143187.7	.411
40	12.0	141754 ± 377	982 ± 31	98.98 ±.06	142211 ± 384	142345.8	.122
41	12.3	140988 ± 375	949 ± 31	99.17 ±.06	141194 ± 382	141508.8	.680
42	12.6	140436 ± 375	923 ± 30	99.05 ±.06	140835 ± 382	140676.7	.171
43	12.9	139564 ± 374	952 ± 31	99.10 ±.06	139863 ± 381	139849.5	.001
44	13.2	139085 ± 373	925 ± 30	99.03 ±.06	139498 ± 380	139027.2	1.531
45	13.5	136842 ± 370	953 ± 31	99.16 ±.06	137028 ± 377	138209.8	9.849
46	13.8	136902 ± 370	976 ± 31	98.99 ±.06	137291 ± 378	137397.1	.078
47	14.1	136479 ± 369	933 ± 31	99.05 ±.06	136827 ± 377	136589.2	.397
48	14.4	135673 ± 368	971 ± 31	99.17 ±.06	135815 ± 375	135786.1	.006
49	14.7	134501 ± 367	985 ± 31	99.03 ±.06	134803 ± 374	134987.7	.244
50	15.0	133634 ± 366	1013 ± 32	98.99 ±.06	133964 ± 373	134194.0	.381
51	15.3	133730 ± 366	1018 ± 32	99.08 ±.06	133935 ± 373	133404.9	2.022
52	15.6	132525 ± 364	1002 ± 32	98.98 ±.06	132861 ± 372	132620.5	.418
53	15.9	131501 ± 363	1015 ± 32	98.96 ±.06	131845 ± 370	131840.7	.000
54	16.2	130623 ± 361	945 ± 31	98.95 ±.06	131039 ± 369	131065.5	.005
55	16.5	130452 ± 361	995 ± 32	98.95 ±.06	130810 ± 369	130294.9	1.952
56	16.8	129246 ± 360	946 ± 31	98.94 ±.06	129654 ± 367	129528.8	.117
57	17.1	128667 ± 359	922 ± 30	99.08 ±.06	128914 ± 365	128767.1	.161
58	17.4	127814 ± 358	935 ± 31	99.08 ±.06	128040 ± 364	128010.0	.007
59	17.7	126560 ± 356	1003 ± 32	99.11 ±.06	126667 ± 362	127257.3	2.657
60	18.0	125995 ± 355	953 ± 31	98.92 ±.07	126395 ± 363	126509.1	.099
61	18.3	125221 ± 354	959 ± 31	98.92 ±.07	125605 ± 362	125765.2	.197
62	18.6	124952 ± 353	966 ± 31	99.03 ±.06	125186 ± 361	125025.7	.197
63	18.9	124570 ± 353	1092 ± 33	98.96 ±.06	124761 ± 361	124290.6	1.703
64	19.2	123728 ± 352	1020 ± 32	99.02 ±.06	123907 ± 359	123559.7	.935
65	19.5	122549 ± 350	1079 ± 33	98.91 ±.07	122792 ± 358	122833.2	.013

Bin #	t^* (ns)	$N \pm \delta N$ (Events/0.3ns)	$B \pm \delta B$ (Events/0.3ns)	$\epsilon \pm \delta\epsilon$ (%)	$S \pm \delta S$ (Events/0.3ns)	f (Events/0.3ns)	$\chi^2(i)$
66	19.8	121920 ± 349	1039 ± 32	98.94 ± .07	122160 ± 357	122111.0	.019
67	20.1	120923 ± 348	1069 ± 33	99.06 ± .06	120970 ± 355	121393.0	1.424
68	20.4	120685 ± 347	1064 ± 33	98.97 ± .06	120849 ± 355	120679.2	.228
69	20.7	119587 ± 346	1107 ± 33	98.90 ± .07	119781 ± 354	119969.6	.284
70	21.0	119428 ± 346	1110 ± 33	99.04 ± .06	119448 ± 353	119264.2	.272
71	21.3	118755 ± 345	1026 ± 32	98.94 ± .07	118976 ± 352	118562.9	1.379
72	21.6	118086 ± 344	1055 ± 32	98.84 ± .07	118391 ± 352	117865.8	2.230
73	21.9	116955 ± 342	1104 ± 33	98.91 ± .07	117115 ± 350	117172.8	.027
74	22.2	116861 ± 342	1103 ± 33	98.90 ± .07	117031 ± 350	116483.8	2.451
75	22.5	115546 ± 340	1179 ± 34	98.88 ± .07	115645 ± 348	115798.9	.195
76	22.8	115146 ± 339	1287 ± 36	98.87 ± .07	115136 ± 348	115118.0	.003
77	23.1	114283 ± 338	1227 ± 35	98.87 ± .07	114333 ± 346	114441.1	.098
78	23.4	114414 ± 338	1400 ± 37	98.91 ± .07	114243 ± 346	113768.2	1.881
79	23.7	112816 ± 336	1380 ± 37	98.82 ± .07	112744 ± 345	113099.3	1.061
80	24.0	112163 ± 335	1449 ± 38	98.91 ± .07	111914 ± 343	112434.3	2.301
81	24.3	112135 ± 335	1568 ± 40	98.99 ± .07	111668 ± 343	111773.1	.093
82	24.6	110773 ± 333	1708 ± 41	98.82 ± .07	110342 ± 342	111115.9	5.114
83	24.9	110973 ± 333	1818 ± 43	98.85 ± .07	110398 ± 342	110462.6	.036
84	25.2	110308 ± 332	1998 ± 45	98.57 ± .08	109854 ± 343	109813.1	.014
85	25.5	109617 ± 331	2190 ± 47	98.75 ± .07	108755 ± 341	109167.4	1.459
86	25.8	108966 ± 330	2420 ± 49	98.45 ± .08	108184 ± 342	108525.5	.996
87	26.1	109273 ± 331	2503 ± 50	98.55 ± .07	108301 ± 342	107887.4	1.467
88	26.4	107679 ± 328	2866 ± 54	98.34 ± .08	106538 ± 341	107253.0	4.393
89	26.7	107796 ± 328	3093 ± 56	98.26 ± .08	106511 ± 342	106622.4	.105
90	27.0	106992 ± 327	3422 ± 58	98.31 ± .08	105302 ± 341	105995.4	4.142
91	27.3	106398 ± 326	3754 ± 61	98.10 ± .08	104579 ± 341	105372.2	5.399
92	27.6	105091 ± 324	4329 ± 66	98.00 ± .08	102752 ± 341	104752.6	34.482
93	27.9	103777 ± 322	4951 ± 70	97.63 ± .09	101149 ± 342	104136.7	76.472
94	28.2	103274 ± 321	5511 ± 74	97.57 ± .09	100115 ± 342	103524.4	99.409
95	28.5	101892 ± 319	5955 ± 77	97.31 ± .10	98494 ± 342	102915.6	167.339
96	28.8	99282 ± 315	6137 ± 78	97.10 ± .10	95836 ± 339	102310.5	364.972
97	29.1	98350 ± 314	6318 ± 79	96.32 ± .12	95448 ± 342	101708.9	335.174
98	29.4	96880 ± 311	6338 ± 80	95.89 ± .13	94320 ± 342	101110.9	394.679
99	29.7	95090 ± 308	6667 ± 82				
100	30.0	93954 ± 307	6484 ± 81				
101	30.3	92802 ± 305	6500 ± 81				
102	30.6	88777 ± 298	6642 ± 81				
103	30.9	83278 ± 289	6834 ± 83				
104	31.2	75993 ± 276	6618 ± 81				
105	31.5	68848 ± 262	6382 ± 80				
106	31.8	63282 ± 252	5921 ± 77				
107	32.1	57381 ± 240	5512 ± 74				
108	32.4	53370 ± 231	5287 ± 73				
109	32.7	49253 ± 222	5031 ± 71				
110	33.0	45428 ± 213	4696 ± 69				